JCB Journal of Cell Biology

ARTICLE

Plastin 3 rescues cell surface translocation and activation of TrkB in spinal muscular atrophy

Luisa Hennlein[1], Hanaa Ghanawi[1]*, Florian Gerstner[2]*, Eduardo Palominos García[1], Ezgi Yildirim[1], Lena Saal-Bauernschubert[1], Mehri Moradi[1], Chunchu Deng[1], Teresa Klein[3], Silke Appenzeller[4], Markus Sauer[3], Michael Briese[1], Christian Simon[2], Michael Sendtner[1], and Sibylle Jablonka[1]

Plastin 3 (PLS3) is an F-actin-bundling protein that has gained attention as a modifier of spinal muscular atrophy (SMA) pathology. SMA is a lethal pediatric neuromuscular disease caused by loss of or mutations in the *Survival Motor Neuron 1* (*SMN1*) gene. Pathophysiological hallmarks are cellular maturation defects of motoneurons prior to degeneration. Despite the observed beneficial modifying effect of PLS3, the mechanism of how it supports F-actin-mediated cellular processes in motoneurons is not yet well understood. Our data reveal disturbed F-actin-dependent translocation of the Tropomyosin receptor kinase B (TrkB) to the cell surface of Smn-deficient motor axon terminals, resulting in reduced TrkB activation by its ligand brain-derived neurotrophic factor (BDNF). Improved actin dynamics by overexpression of hPLS3 restores membrane recruitment and activation of TrkB and enhances spontaneous calcium transients by increasing $Ca_v2.1/2$ "cluster-like" formations in SMA axon terminals. Thus, our study provides a novel role for PLS3 in supporting correct alignment of transmembrane proteins, a key mechanism for (moto)-neuronal development.

Introduction

Proximal spinal muscular atrophy (SMA) is the most common form of motoneuron diseases in children and young adults, which is caused by the deficiency of the SMN protein (Lefebvre et al., 1997). Although genetic therapies have been successfully applied to SMA patients, it remains enigmatic how SMN loss affects cellular differentiation and maturation of motoneurons and why it can be compensated by SMA modifying proteins such as Plastin 3 (PLS3; Oprea et al., 2008). Primary motoneurons from SMA type I mouse models exhibit reduced β-actin levels that result in decreased growth cone size and impaired axon elongation (Jablonka et al., 2007; Moradi et al., 2017; Nölle et al., 2011; Rossoll et al., 2003; Saal et al., 2014). Furthermore, disturbed accumulation of the voltage-gated calcium channels (VGCCs) $Ca_v2.1/2$ coincides with reduced spontaneous Ca^{2+} transients (Jablonka et al., 2007) and neurotransmission defects in SMA mice (Tejero et al., 2020; Tejero et al., 2016). Since the orchestration of the presynaptic compartment depends on a well-organized cytoskeleton, decreased $Ca_v2.1/2$ cluster formations imply impaired localization of further transmembrane proteins in SMA axon terminals.

The functional deficiency of Tropomyosin receptor kinase B (TrkB), the high-affinity receptor for brain-derived neurotrophic factor (BDNF; Chao and Hempstead, 1995; Ebendal, 1992; Reichardt, 2006), causes disturbed differentiation of primary motoneurons (Dombert et al., 2017). Neurotrophic factor signaling activates various signaling pathways indispensable for motoneuron survival and differentiation (Arakawa et al., 1990; Henderson et al., 1994; Hughes et al., 1993; Pennica et al., 1996; Reichardt, 2006; Sendtner et al., 1992a; Sendtner et al., 1992b). The morphological and functional alterations under TrkB kinase domain-deficient conditions such as impaired motoneuron differentiation and reduced spontaneous Ca^{2+} transients phenocopy those observed in SMA motoneurons (Dombert et al., 2017; Jablonka et al., 2007; Rossoll et al., 2003). This inevitably raises the question of whether BDNF/TrkB signaling is altered in SMA. The affected cytoskeleton and unbalanced F- to G-actin ratio in Smn-deficient motoneurons (Jablonka et al., 2007; Moradi et al., 2017; Nölle et al., 2011; Rossoll et al., 2003; Saal et al., 2014) suggest that BDNF/TrkB signaling could be modified through

[1]Institute of Clinical Neurobiology, University Hospital Würzburg, Würzburg, Germany; [2]Carl-Ludwig-Institute for Physiology, Leipzig University, Leipzig, Germany; [3]Department of Biotechnology and Biophysics, Biocenter, Julius-Maximilians-University Würzburg, Würzburg, Germany; [4]Comprehensive Cancer Center Mainfranken; Core Unit Bioinformatics, University Hospital Würzburg, Würzburg, Germany.

*H. Ghanawi and F. Gerstner contributed equally to this paper. Correspondence to Sibylle Jablonka: jablonka_s@ukw.de

H. Ghanawi's current affiliation is Department of Pharmacy, Center for Drug Research, Ludwig-Maximilians-Universität München, München, Germany. L. Saal-Bauernschubert's current affiliation is Department of Anaesthesiology, Intensive Care, Emergency and Pain Medicine, University Hospital Würzburg, Würzburg, Germany.

F-actin assembly by modulating proteins such as PLS3. PLS3 associates with the F-actin cytoskeleton within filopodia, where it supports F-actin bundling (Garbett et al., 2020; Giganti et al., 2005) and thus strengthens the protrusive actin network (Garbett et al., 2020). Transcriptome-wide differential expression analysis from *SMN1*-deleted siblings with discordant disease outcomes revealed a significant association between disease severity and PLS3 expression in female SMA patients (Oprea et al., 2008).

Here, we showed reduced levels and impaired BDNF-induced phosphorylation of TrkB within axon terminals of Smn-deficient motoneurons in vitro and in the neuromuscular junction (NMJ) of a severe SMA mouse model. Virus-mediated human PLS3 (hPLS3) overexpression in cultured SMA motoneurons resulted in a significant rescue of F-actin dynamics that corresponds to improved TrkB translocation and its activation through BDNF. Beyond that, spontaneous Ca^{2+} transients due to improved $Ca_v2.1/2$ "cluster-like" formations can be restored to wild-type level in vitro. Hence, our study highlights that the affected actin cytoskeleton due to PLS3 downregulation in SMA motoneurons modulates neurotrophic factor signaling and spontaneous Ca^{2+} influx that is crucial for proper cellular differentiation, such as axon elongation and growth cone morphology and functional maintenance of motoneurons.

Results

Smn-deficient axon terminals exhibit reduced TrkB protein levels and impaired BDNF-induced TrkB phosphorylation

In order to investigate whether BDNF/TrkB signaling is disturbed upon Smn deficiency and could therefore contribute to SMA pathology, we analyzed NMJs in the affected *Transversus abdominis anterior* (TVA) muscle of the *SMNΔ7* mouse model (Tejero et al., 2016; Torres-Benito et al., 2011) and in growth cones of cultured primary motoneurons of *Smn*$^{-/-}$;*SMN2* mouse embryos. For this purpose, NMJs were analyzed at an early symptomatic stage at postnatal day (P) 5 and a later symptomatic stage at P10-11. Consistent with previous studies (Hosseinibarkooie et al., 2016; Ruiz et al., 2010; Tejero et al., 2020; Tejero et al., 2016), the total presynaptic area as well as the ratio of presynaptic and postsynaptic areas was significantly reduced in *SMNΔ7* pups at P10-11 (Fig. S1 A). To determine TrkB localization and activation at axon terminals, we performed immunostainings with TrkB and phosphorylated TrkB (p-TrkB) antibodies. Specificity was verified by analysis of *Ntrk2*$^{-/-}$ NMJs at P5 (Fig. S2 A) and growth cones of cultured motoneurons from *Ntrk2*$^{-/-}$ mouse embryos (Fig. S2, B–D). In *SMNΔ7* presynaptic terminals, the total TrkB levels were markedly decreased already at P5 (Fig. S1 B), and this became even more pronounced (~50%) during disease progression at P10-11 (Fig. 1 A). Interestingly, SMA motoneurons showed only a moderate but significant loss in total TrkB levels in growth cones (Fig. 1 B). In whole-cell extracts, transcript quantification through RT-PCR (Fig. 1 C) and Western blot analysis (Fig. S1 C) did not show any differences in TrkB levels between Smn-deficient and control motoneurons. These results suggest that alterations in TrkB localization exclusively relate to cellular dysregulations in axon terminals of SMA motoneurons.

To examine the activation of the receptor upon stimulation with its ligand, p-TrkB immunostainings were performed on TVA muscle explants that were BDNF-stimulated for 30 min prior to fixation. At P10-11, significantly reduced levels of p-TrkB have been observed, and BDNF stimulation could not evoke a raise in p-TrkB signals in *SMNΔ7* mice (Fig. 1 D). Although significantly decreased levels of p-TrkB have been observed already at P5, BDNF treatment could still evoke a marked increase of p-TrkB in the endplates of early symptomatic *SMNΔ7* mice (Fig. S1 D). In contrast to Western blot analysis of whole-cell extracts (Fig. S1 C), immunocytochemical analysis of Smn-deficient growth cones revealed an impaired BDNF-induced TrkB phosphorylation in comparison with control growth cones (Fig. 1 E). To examine whether the alterations of the actin cytoskeleton in SMA axon terminals are involved in the affected TrkB phosphorylation, motoneurons were treated with the mycotoxin Cytochalasin D (CytoD) prior to BDNF stimulation to inhibit actin polymerization. The analysis of p-TrkB in axon terminals revealed that the BDNF-induced TrkB activation is absent upon CytoD pre-treatment (Fig. 1 F). Hence, the disruption of the cytoskeleton phenocopies Smn deficiency and seems to be causative for the impaired TrkB activation. Collectively, these data argue that loss of Smn interferes with localization and activation of TrkB in the axon terminals and motor endplates that consequently could lead to failures in the BDNF/TrkB-signaling cascade.

Cyclic AMP-induced TrkB surface recruitment through actin filaments is impaired in Smn-deficient axon terminals

To examine the possibility that the impaired TrkB activation is due to altered receptor presentation at the cell surface, a live-staining protocol was established to label TrkB exclusively localized at the cell surface (see Materials and methods). No differences were observed in baseline TrkB surface levels in Smn-deficient motoneurons compared to controls (Fig. 2 A, first lane). Next, we studied whether endocytosis of the receptor upon BDNF stimulation is disturbed in Smn-deficient axon terminals. Therefore, cultured motoneurons were stimulated with BDNF for 5 min and 15 min. TrkB disappears from the cell surface following BDNF stimulation in a time-dependent manner in control motoneurons, and similar observations were made for SMA growth cones (Fig. 2 A). Thus, BDNF-mediated TrkB internalization is not altered in SMA motoneurons. Early studies with motoneurons have shown that cyclic AMP (cAMP) is one of the key regulators of TrkB surface presentation and therefore modulates the responsiveness to BDNF (Du et al., 2000; Meyer-Franke et al., 1998). To investigate this mechanism in SMA motoneurons, we used cAMP to stimulate TrkB transfer to the plasma membrane. Indeed, a 20 min 8-CPT-cAMP stimulation was sufficient to induce a robust elevation of TrkB at the cell surface of control motoneurons. However, no shift in TrkB translocation to the plasma membrane was observed in Smn-deficient growth cones (Fig. 2 B). The failure of 8-CPT-cAMP to recruit TrkB to the cell surface in SMA motoneurons could be caused by a defective actin cytoskeleton. To address this possibility, motoneurons were pre-treated with CytoD prior to 8-CPT-cAMP stimulation that prevented the cAMP-induced TrkB

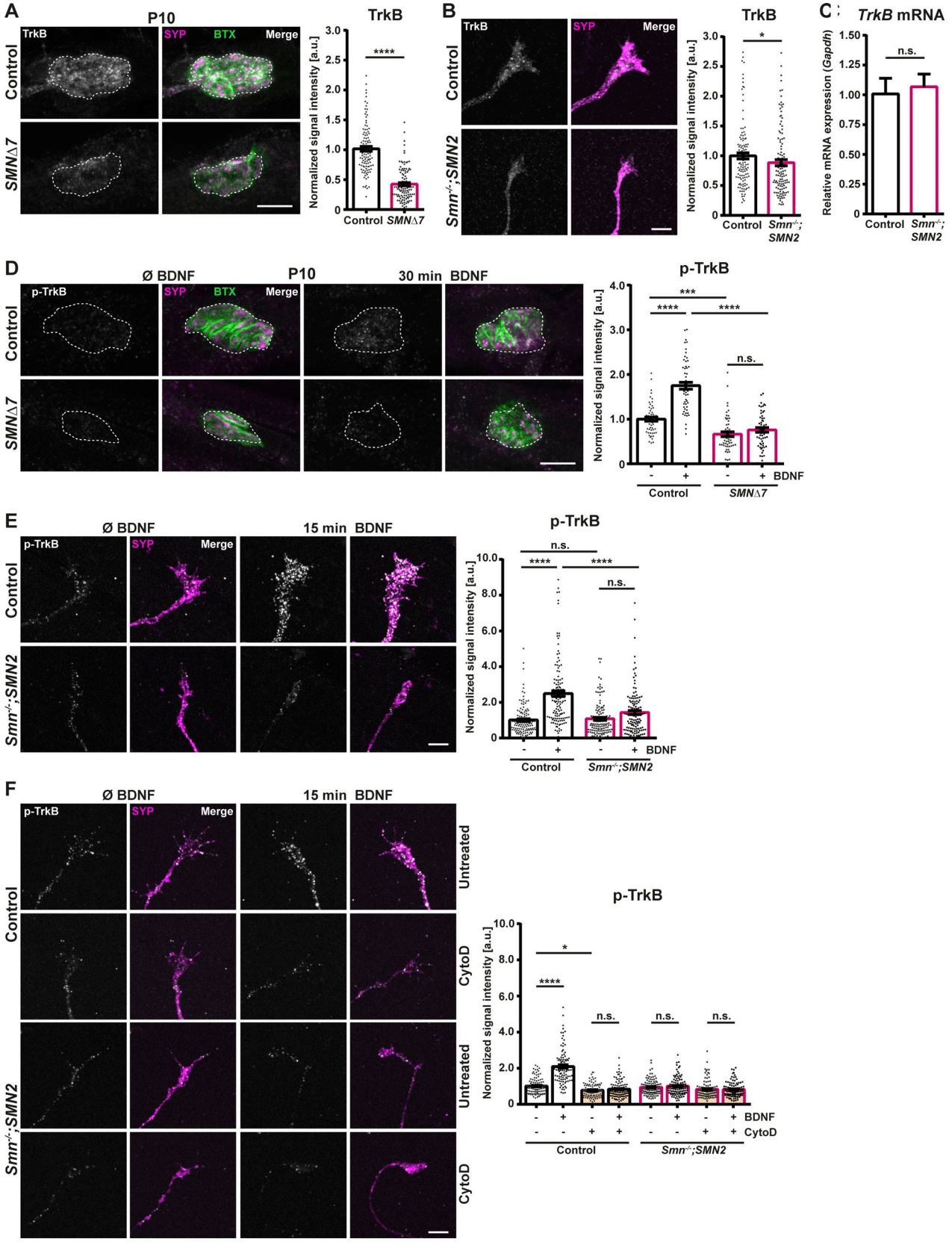

Figure 1. **TrkB localization and its activation upon BDNF stimulation are impaired in Smn-deficient axon terminals. (A)** NMJs in the *Transversus abdominis anterior* (TVA) muscle in control and *SMNΔ7* P10 animals stained against TrkB (gray), Synaptophysin-1 (SYP, magenta), and postsynaptic ACh receptors (Bungarotoxin [BTX], green); scale bar: 10 µm. Dotted line depicts outline of the presynapse (SYP signal). Normalized mean gray values of TrkB (N = 5, *n* = 109; U-Mann–Whitney, ****P ≤ 0.0001). **(B)** Control and *Smn*$^{-/-}$;*SMN2* growth cones stained against TrkB (gray) and SYP (magenta); scale bar: 5 µm. Normalized

mean gray values of TrkB (N = 6, *n* = 120; U-Mann–Whitney, *P = 0.0204). Bar represents the mean ± SEM. **(C)** Relative expression of *TrkB* in whole-cell lysates from control and *Smn*$^{-/-}$;*SMN2* motoneurons. Quantification of *TrkB* relative to *Gapdh* (N = 3, *n* = 7; U-Mann–Whitney). Data are presented as mean ± SD. **(D)** NMJs in the TVA muscle in control and *SMNΔ7* P10 animals unstimulated and 30 min BDNF stimulated stained against p-TrkB (gray), SYP (magenta), and BTX (green), scale bar: 10 µm. Dotted line depicts outline of the presynapse (SYP signal). Normalized mean gray values of p-TrkB (N = 4, *n* = 56; ANOVA Kruskal–Wallis, ***P ≤ 0.001; ****P ≤ 0.0001). **(E)** Control and *Smn*$^{-/-}$;*SMN2* growth cones unstimulated and 15 min BDNF stimulated stained against p-TrkB (gray) and SYP (magenta); scale bar: 5 µm. Normalized mean gray values of p-TrkB (N = 6, *n* = 130; ANOVA Kruskal–Wallis, ****P ≤ 0.0001). **(F)** Control and *Smn*$^{-/-}$;*SMN2* growth cones unstimulated and 15 min BDNF stimulated that were pre-treated with 0.5 µM Cytochalasin D (CytoD) stained against p-TrkB (gray) and SYP (magenta), scale bar: 5 µm. Normalized mean gray values of p-TrkB (N = 3, *n* = 105; ANOVA Kruskal–Wallis, *P ≤ 0.05; ****P ≤ 0.0001). Data are presented as scatter dot plot with bar. Bar represents the mean ± SEM (except for C).

surface translocation in control motoneurons, while no further effect could be observed in Smn-deficient cells (Fig. 2 C). Thus, our experiments demonstrate that the ligand-induced TrkB internalization in SMA motoneurons is unaffected but the cAMP-mediated TrkB recruitment to the cell surface through actin filaments is impaired.

Transcriptome analysis reveals a downregulation of *Pls3* mRNA in the somatodendritic and axonal compartment of Smn-deficient motoneurons

In order to explore compartment-specific transcript alterations that relate to the dysregulated actin cytoskeleton and therefore could be relevant for defective TrkB translocation and activation, we performed RNA sequencing (RNA-seq) of Smn knockdown (sh*Smn*) motoneurons (Fig. 3 A) cultured in compartmentalized microfluidic chambers. The differential gene expression analysis (Table S1) revealed a variety of transcripts that showed altered expression upon Smn knockdown in the somatodendritic and the axonal compartment compared to the GFP-expressing controls (Fig. 3 B). 604 transcripts showed a significant (P < 0.05) down- or upregulation in the somatodendritic compartment, whereas 521 transcripts were significantly down- or upregulated in the axonal compartment of Smn-deficient motoneurons (Fig. 3 C), with an intersection of 132 transcripts from both compartments (Fig. 3, C and D; and Table S1). We further used Gene Ontology (GO)-term analysis to examine pathways potentially altered in the two compartments (Fig. 3 E and Table S2) of Smn knockdown motoneurons. Interestingly, ATP- and oxidative phosphorylation-related genes are upregulated in both compartments, while especially GTP-linked and microtubule-associated candidate transcripts are downregulated in the somatodendritic compartment (Fig. 3 E and Table S2). Only in the axonal compartment, transcripts encoding proteins with functions related to the actin cytoskeleton appear to be downregulated in Smn-deficient motoneurons (Fig. 3, E–G). Within the top 10 of axonal downregulated actin-related transcripts (Fig. 3, F and G, yellow underlay) we identified the actin-modulator *Pls3* (Fig. 3, F–H). Different levels of PLS3 are a characteristic feature in *SMN1*-deleted siblings with discordant disease severity (Oprea et al., 2008). Pls3 is a potent actin-bundler required for F-actin stability (Karpova et al., 1995; Shinomiya, 2012). The importance of a stabilized actin cytoskeleton for correct trafficking of the presynaptic ER or vesicles derived from the ER was already shown (Deng et al., 2021). Thus, the reduced levels of Pls3 might interfere with correct translocation of transmembrane proteins such as TrkB. In addition to this, *Arpc1b*, a component of the actin-related 2/3 (Arp2/3) complex, which is important for the initiation of actin filament branching (Lee et al., 2010; Suraneni et al., 2012; Welch et al., 1997; Wu et al., 2012a), is also found among the 10 most downregulated actin-related transcripts in the axonal compartment (Fig. 3, F and G). These data indicate that Smn deficiency impacts actin-related transcripts in the axonal compartment.

Pls3-deficient motoneurons show aberrant TrkB localization and activation comparable to Smn-deficient motoneurons

As RNA-seq data revealed that the actin-bundling protein Pls3, the most relevant genetic SMA modifier, is markedly decreased in the axonal compartment of Smn knockdown motoneurons, we asked whether a lack of Pls3 could be involved in impaired TrkB localization and activation in axon terminals of Smn-deficient motoneurons. Quantification of the Pls3 immunosignal within growth cones confirmed the RNA-seq data of Smn knockdown motoneurons, since *Smn*$^{-/-}$;*SMN2* growth cones showed a significant reduction of Pls3 (Fig. 4 A). To test whether Pls3 is involved in actin-related processes modulating the translocation and activation of TrkB, we used a shRNA approach to target the endogenous *Pls3* (sh*Pls3*) and used *Luciferase*-shRNA (sh*Luci*) as control. Quantitative transcript analysis through RT-PCR confirmed a knockdown efficiency of ∼60% in motoneurons transduced with the sh*Pls3*-harboring lentivirus (Fig. 4 B). Morphological analysis revealed that, like SMA motoneurons (Jablonka et al., 2007), the axons of Pls3 knockdown cells cultured on laminin-221/211 exhibited altered elongation (Fig. 4 C) as well as reduced growth cone size (Fig. 4 D). Since PLS3 acts as an F-actin-bundling protein, we used live-cell imaging to assess how the reduced Pls3 levels modulate actin dynamics. For this purpose, cultured Pls3 knockdown motoneurons were incubated with a fluorescent F-actin binding probe (SiR-actin) to visualize actin movements over a period of 20 min (Fig. 4, E–G). Quantification of the SiR-actin signal revealed that Pls3 knockdown motoneurons display impaired actin movements in the growth cone, as shown by reduced moving distance of single filopodia (Fig. 4 E) and decreased velocity of the movements (Fig. 4 F). To examine BDNF/TrkB signaling in these neurons, we investigated the TrkB localization in Pls3-depleted growth cones. Interestingly, we found significantly reduced total TrkB levels (Fig. 4 H). Comparison of the ligand-induced immunosignal of p-TrkB after 15 min BDNF stimulation revealed that, comparable to Smn-deficient neurons, the activation of the receptor is impaired (Fig. 4 I). Next, we examined the responsiveness to BDNF and cAMP stimulation of receptors presented at the cell surface. In our live-staining assay, we observed preserved baseline surface TrkB levels and an intact TrkB

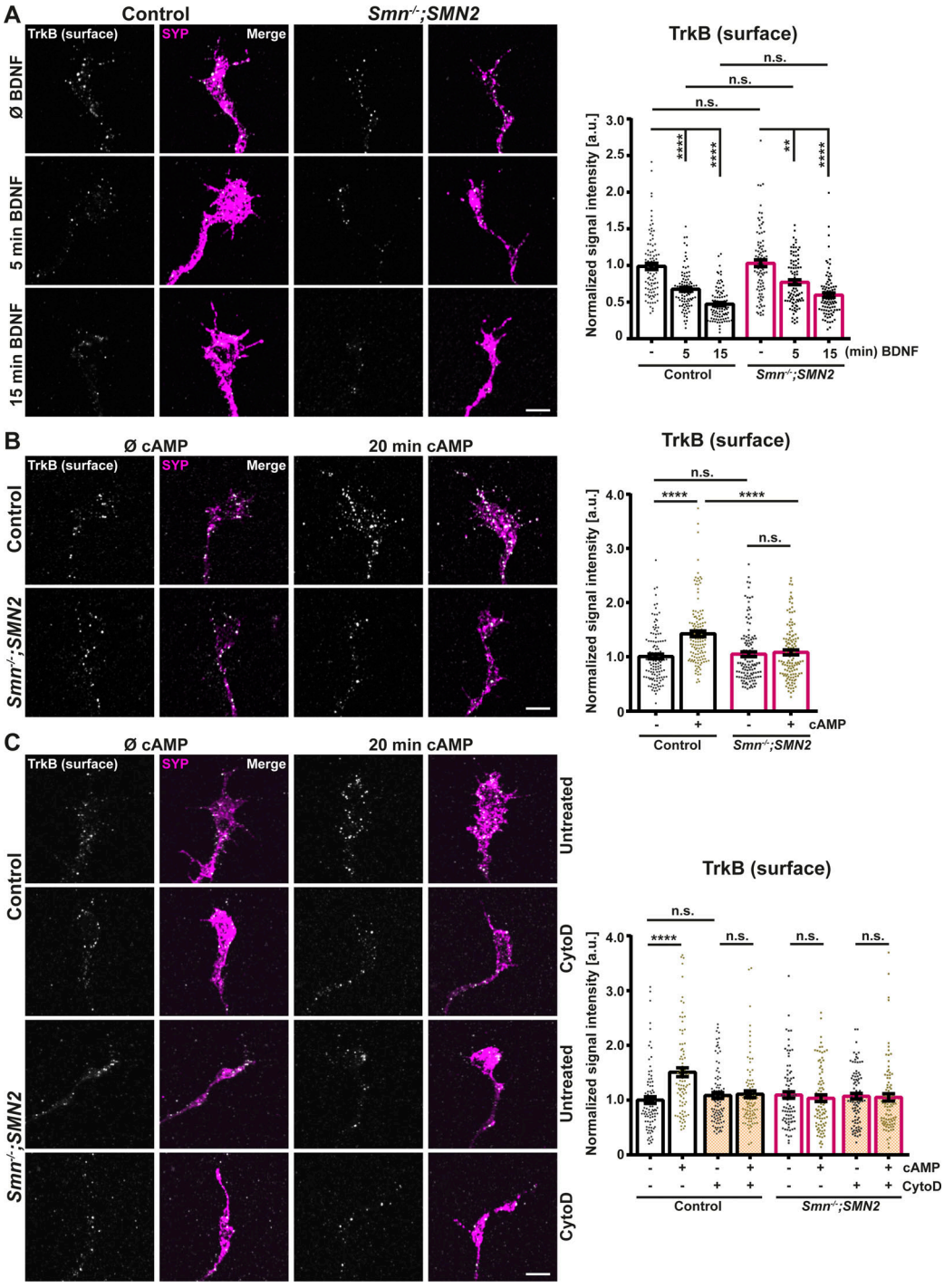

Figure 2. **Actin-dependent cAMP-induced TrkB surface recruitment is impaired in Smn-deficient motoneuron growth cones. (A–C)** Growth cones from control and *Smn*$^{-/-}$;*SMN2* motoneurons stained against surface TrkB (gray) and Synaptophysin-1 (SYP, magenta). Scale bars: 5 µm. **(A)** Normalized mean gray values of surface TrkB in control and *Smn*$^{-/-}$;*SMN2* terminals unstimulated and stimulated for 5 min and 15 min BDNF (N = 3, *n* = 93; ANOVA Kruskal–Wallis, **P ≤ 0.01; ****P ≤ 0.0001). **(B)** Normalized mean gray values of surface TrkB in control and *Smn*$^{-/-}$;*SMN2* terminals unstimulated and 20 min 8-CPT-cAMP stimulated (N = 4, *n* = 125; ANOVA Kruskal–Wallis, ****P ≤ 0.0001). **(C)** Normalized mean gray values of surface TrkB in control and *Smn*$^{-/-}$;*SMN2* terminals treated with 0.5 µM Cytochalasin D (CytoD) prior to 20 min 8-CPT-cAMP stimulation (N = 3, *n* = 90; ANOVA Kruskal–Wallis, ****P ≤ 0.0001). Data are presented as scatter dot plot with bar. Bars represent the mean ± SEM.

endocytosis upon 15 min BDNF stimulation (Fig. 4 J). However, we did not monitor any 8-CPT-cAMP-induced TrkB surface recruitment in Pls3-deficient motoneurons (Fig. 4 J). In conclusion, these experiments imply that Pls3 is functionally participating in the dynamic surface presentation of TrkB and its activation through BDNF stimulation.

Based on these results, we then hypothesized that the membrane translocation and accumulation of VGCCs at presynaptic

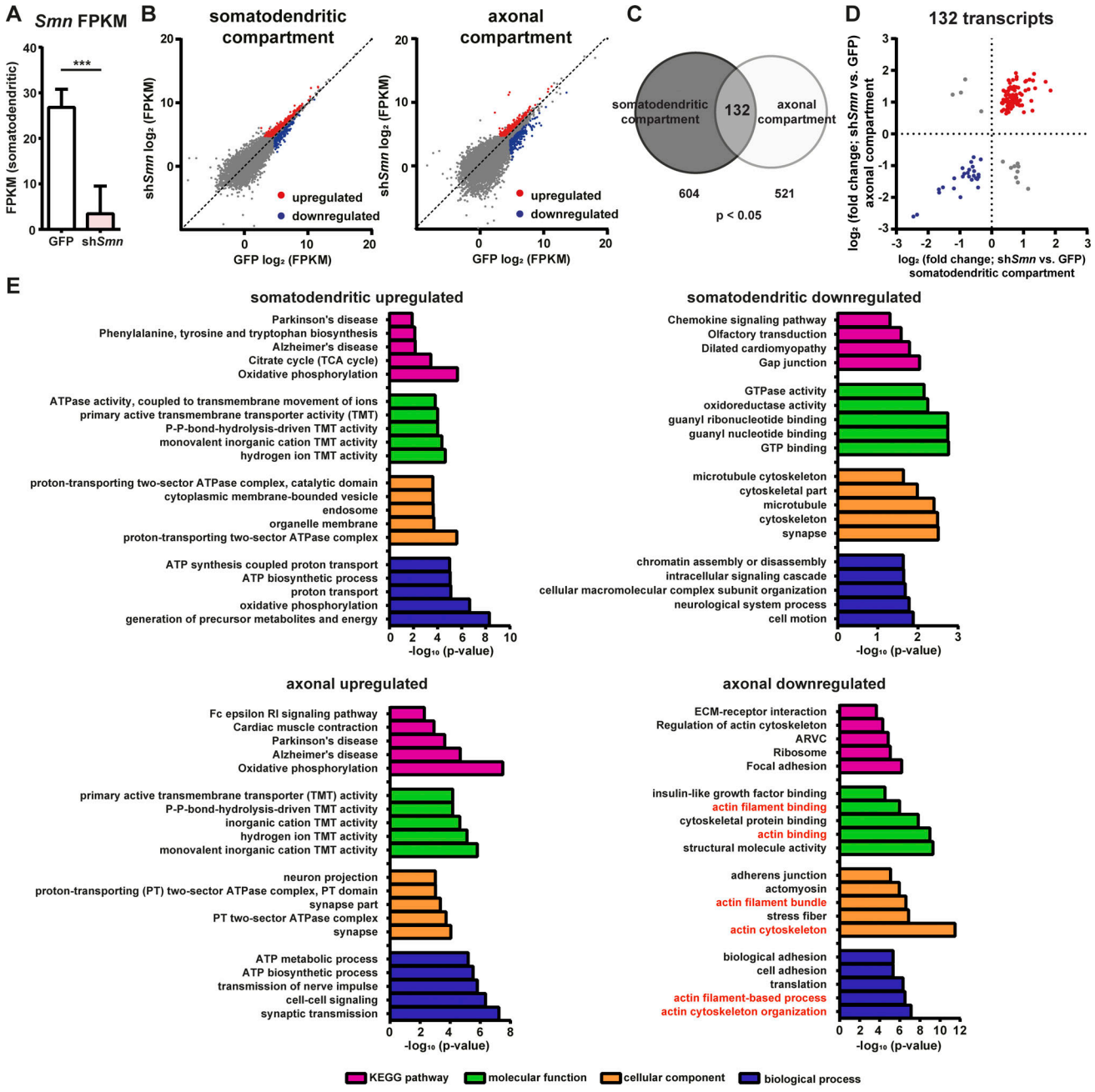

Gene	FPKM (GFP)	FPKM (shSmn)	log₂ (fold change)		Gene	FPKM (GFP)	FPKM (shSmn)	log₂ (fold change)
Csrp1	106.805	8.25855	-3.69294		*Actn4*	129.98	43.0336	-1.59475
Cnn2	79.61	11.6607	-2.7713		*Tpm4*	62.0042	21.0126	-1.56111
Acta2	645.657	106.194	-2.60406		*Shroom3*	26.9435	9.51785	-1.50123
Arpc1b	**31.0864**	**5.16692**	**-2.58891**		*Epb4.1l2*	26.5867	9.61983	-1.46662
Vcl	27.5321	5.22346	-2.39804		*Cnn3*	137.529	51.2909	-1.42296
Anxa2	92.3174	18.702	-2.30341		*Tpm1*	225.139	85.5834	-1.39542
Pls3	**33.8872**	**7.21694**	**-2.23128**		*Mprip*	37.7798	14.9946	-1.33317
Actn1	93.2633	19.8757	-2.2303		*Parva*	30.2491	12.1267	-1.3187
Flna	452.547	100.704	-2.16795		*Myh10*	87.2478	36.3765	-1.26211
Lima1	34.6953	7.76953	-2.15884		*Pdlim7*	70.3618	29.5404	-1.25211
Gm8399	79.5941	18.087	-2.13771		*Cit*	27.5221	12.0879	-1.18703
Myl9	104.346	24.8712	-2.06883		*Fat1*	58.6661	25.8203	-1.18402
Lasp1	317.983	78.6573	-2.0153		*Arpc4.Ttll3*	26.7441	13.5745	-0.978318
Jup	29.4994	7.40543	-1.99403		*Itgb1*	85.0981	43.3472	-0.973187
Myh9	149.333	38.7639	-1.94575		*Myo18a*	35.1211	18.1677	-0.950962
Fscn1	157.637	43.7493	-1.84928		*Coti1*	66.5893	35.4652	-0.908888
Flnb	45.6083	13.4336	-1.76345		*Pfn1*	305.387	166.75	-0.872952
Ctnna1	38.9833	11.9366	-1.70747		*Gm12715*	31.7078	18.1015	-0.80873
Cald1	119.616	39.3223	-1.60499					

Figure 3. **RNA-seq analysis of compartmentalized Smn-deficient motoneurons. (A)** Values of fragments per kilobase of transcript per million mapped reads (FPKM) measured by RNA-seq of the somatodendritic compartment of GFP controls and Smn knockdown motoneurons (n = 4/6, Two-tailed unpaired t test, ***P ≤ 0.001). Data are presented as mean ± SD. **(B)** Scatter plots of logarithmized FPKM values derived from cuffdiff analysis of Smn knockdown versus

GFP-expressing control motoneurons within the somatodendritic and axonal compartment. Red dots represent significantly ($P \leq 0.05$) upregulated transcripts while blue marked genes are significantly ($P \leq 0.05$) downregulated. **(C)** Venn diagram of genes down- and upregulated in the somatodendritic and the axonal compartment with an intersection of 132 transcripts from both compartments. **(D)** Log_2 fold changes of the 132 transcripts. **(E)** GO term analysis of transcripts up- or downregulated in the somatodendritic and axonal compartment of Smn knockdown motoneurons. **(F)** Scatter plots of logarithmized FPKMs of actin-related proteins revealed by GO term analysis downregulated in the axonal compartment of Smn knockdown motoneurons. **(G)** FPKM expression values and log_2 fold changes of the actin-related genes which are downregulated in the axonal compartment. Top 10 downregulated transcripts are marked in yellow. **(H)** FPKM values of *Pls3* measured by RNA-seq of the axonal compartment of GFP controls and Smn knockdown motoneurons (n = 4/6; Two-tailed unpaired t test, ***$P \leq 0.001$). Data are presented as mean ± SD.

terminals might as well be actin dependent. Thus, we investigated whether Pls3 knockdown interferes with the localization and function of $Ca_v2.2$ in axon terminals. Quantification of the $Ca_v2.2$ immunosignal in Pls3-deficient growth cones showed significantly reduced levels of $Ca_v2.2$ (Fig. 4 K). Moreover, high resolution Structured Illumination Microscopy (SIM) revealed that the formation of $Ca_v2.2$ "cluster-like" accumulations are markedly diminished upon knockdown of Pls3 (Fig. 4 L, white arrows), similar to Smn-deficient motoneurons. Hence, we asked whether the functionality of the VGCCs is impaired in these neurons. Therefore, we examined the frequency of spontaneous spike-like Ca^{2+} transients in the growth cones of Pls3-depleted motoneurons. Indeed, we found that in contrast to the GFP-expressing control motoneurons, Pls3 knockdown growth cones display reduced spontaneous frequencies of Ca^{2+} transients in their axon terminals (Fig. 4 M). Thus, our data demonstrate that Pls3 is required for the correct alignment and function of other presynaptic transmembrane proteins, such as VGCCs, in addition to TrkB.

Overexpression of hPLS3 enhances TrkB localization and activation in Smn-deficient motor axon terminals

Since Pls3 knockdown and SMA motoneurons show similar defects in axonal elongation, TrkB phosphorylation, cAMP-mediated TrkB surface translocation, and cellular excitability, we studied the effects of hPLS3 overexpression in SMA axon terminals. Smn-deficient motoneurons were transduced with the *human PLS3*-expressing lentivirus (LV-*hPLS3*) or a control virus delivering *mCherry* (LV-*mCh*). Quantitative analysis revealed a robust overexpression of *hPLS3* mRNA (Fig. 5 A). Intriguingly, overexpressing hPLS3 in SMA motoneurons restored impaired axon elongation (Fig. 5 B) and growth cone size (Fig. 5 C) to wild-type levels. In control motoneurons, the overexpression of hPLS3 had no effects on axon growth and differentiation. To study whether elevated hPLS3 levels modulate actin dynamics, we visualized actin movements over a period of 20 min using SiR-actin (Fig. 5, D–F). Quantification of the SiR-actin signal revealed that SMA motoneurons display reduced actin movements in the axon terminals (Fig. 5, D and E). The distance of individual filopodia movements (Fig. 5 D), as well as the velocity of these movements (Fig. 5 E), were significantly enhanced upon hPLS3 overexpression. Analysis of the ratio of F/G-actin revealed that Smn-deficient cells transduced with LV-*mCh* display diminished levels of F-actin, which is reflected by a reduced F/G-actin ratio (Fig. 5 G). Again, overexpression of hPLS3 improved this effect (Fig. 5 G). These data indicate that overexpressing hPLS3 in SMA motoneurons causes marked morphological and functional improvements. We then tested whether the observed TrkB defects are ameliorated as well. Quantification of the TrkB immunofluorescence signal in Smn-deficient cells using confocal microscopy (Fig. 5 H) and SIM (Fig. 5 I) revealed that total TrkB levels are slightly increased upon hPLS3 overexpression. Moreover, we used SIM to study the localization of Pls3 and TrkB along actin filaments in axon terminals. In control motoneurons (LV-*mCh* and LV-*hPLS3* transduced), Pls3 was located along bundled actin filaments (Fig. 5, J and K). However, SIM confirmed previous findings showing reduced levels of F-actin, Pls3, and TrkB in LV-*mCh* transduced SMA motoneurons (Fig. 5 L). Upon overexpression of hPLS3, the morphology of Smn-deficient growth cones reversed back to that resembling control motoneurons. The level of bundled actin filaments is enhanced and showed abundant localization of Pls3 along the filaments (Fig. 5 M). Interestingly, TrkB is mostly located in proximity of Pls3-bundled actin filaments, pointing to a role of these filaments in TrkB surface translocation. Therefore, we checked TrkB expression on the cell surface. Comparison of the baseline surface TrkB levels revealed no differences; however, when hPLS3-overexpressing Smn-deficient motoneurons were treated with 8-CPT-cAMP to induce receptor recruitment to the cell surface, a marked rise of TrkB at the plasma membrane was observed, while no such increase was detectable in LV-*mCh* transduced SMA motoneurons (Fig. 6 A). These findings indicate that the impaired cAMP-induced TrkB membrane translocation can be rescued by hPLS3 overexpression in SMA motoneurons. Further evidence for improved dynamical vesicular TrkB transport upon cAMP stimulation along actin filaments in Smn-deficient motor axons overexpressing hPLS3 is qualitatively documented by Videos 1, 2, and 3. Since hPLS3 overexpression normalizes the distribution of TrkB and its activity-dependent surface translocation, we assessed whether the BDNF-induced TrkB activation is rescued as well. Comparison of the p-TrkB immunosignal after 15 min BDNF stimulation showed that LV-*mCh* transduced Smn-deficient motoneurons did not exhibit increased p-TrkB immunoreactivity. This defect was normalized to control levels when hPLS3 was overexpressed (Fig. 6 B). To test whether TrkB activation leads to functional downstream signal transduction, we investigated the phosphorylation of Akt (p-Akt) upon BDNF stimulation. We could demonstrate that a 15 min BDNF stimulation is sufficient to increase the p-Akt signal in control cells, independent of viral transduction, but was significantly less effective in Smn-deficient motoneurons (Fig. 6 C). However, hPLS3-overexpressing SMA motoneurons showed a much stronger increase of p-Akt upon BDNF stimulation (Fig. 6 C). Taken together, hPLS3 overexpression in SMA motoneurons rescues the localization and cAMP-induced translocation as well

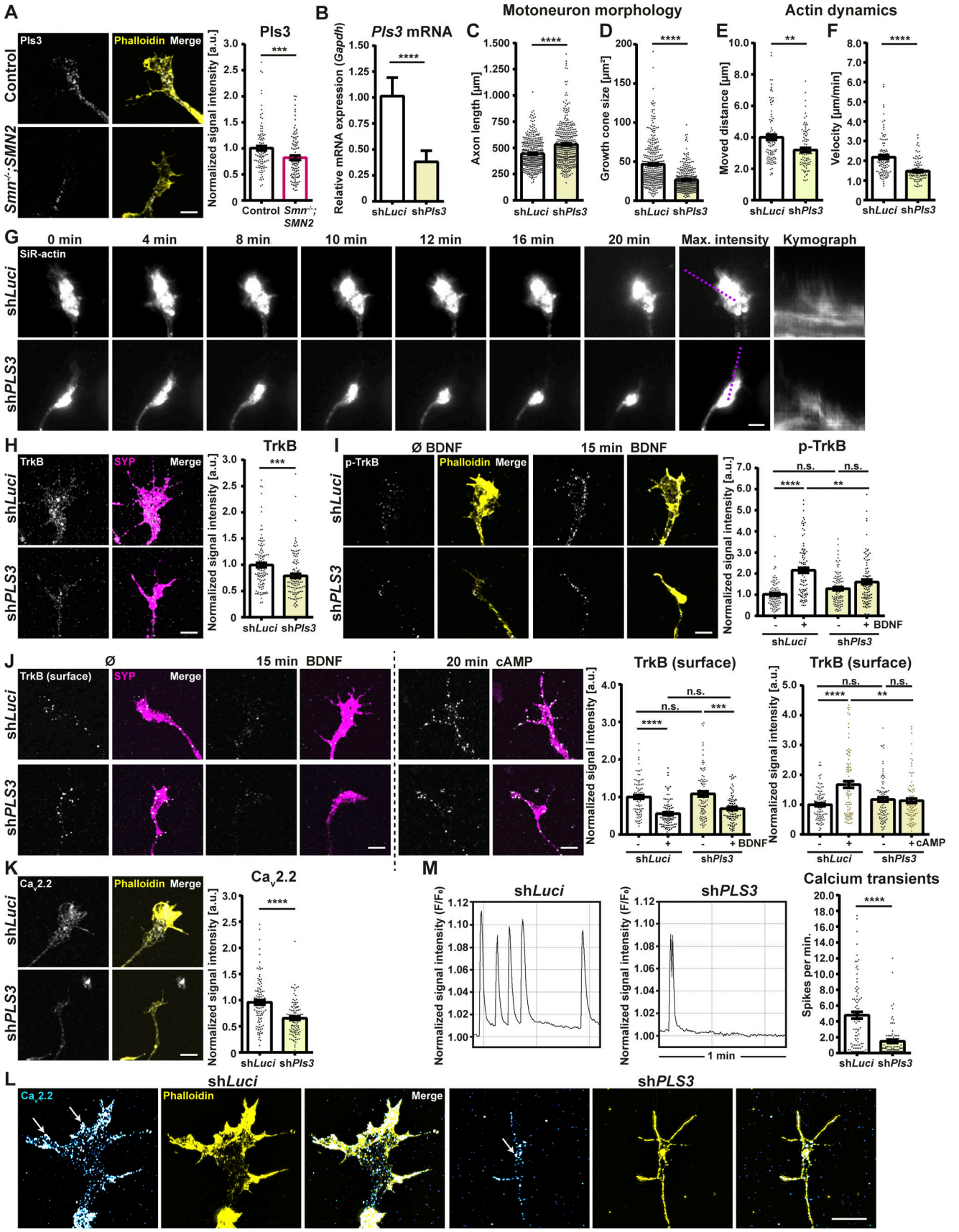

Figure 4. **Pls3 depletion results in morphological changes and aberrant TrkB localization and phosphorylation. (A)** Control and *Smn*$^{-/-}$;*SMN2* growth cones stained against Pls3 (gray) and F-actin (Phalloidin, yellow). Normalized mean gray values of Pls3 (N = 3, *n* = 106; U-Mann–Whitney, ***P = 0.001).

(B) Relative expression of *Pls3* in whole-cell lysates of sh*Luci* and sh*Pls3* motoneurons. Quantification of *Pls3* relative to *Gapdh* (N = 5, *n* = 8; two-tailed unpaired *t* test, ****P ≤ 0.0001). Bars represent the mean ± SD. **(C and D)** Pls3 knockdown results in (C) increased axon length (µm; N = 3; *n* = 400; sh*Luci*: 443.1 ± 6.7 µm, sh*Pls3*: 532.9 ± 9.8 µm; U-Mann–Whitney, ****P ≤ 0.0001) and (D) decreased growth cone size (µm^2; N = 8; *n* = 350; sh*Luci*: 46.48 ± 1.52 µm^2, sh*Pls3*: 26.63 ± 0.77 µm^2; U-Mann–Whitney, ****P ≤ 0.0001). **(E–G)** sh*Luci* and sh*Pls3* growth cones with SiR-actin were monitored for 20 min. ROI (purple dotted line) of a single filopodia with the corresponding kymograph. Quantification of (E) the moved distance (amplitude in µm) of single filopodia (N = 5; *n* = 100; U-Mann–Whitney, **P = 0.0016) and (F) the velocity (distance [µm] over time [min]) of single filopodia (N = 5; *n* = 100; U-Mann–Whitney, ****P ≤ 0.0001). **(H)** sh*Luci* and sh*Pls3* growth cones stained against TrkB (gray) and Synaptophysin-1 (SYP, magenta). Normalized mean gray values of TrkB (N = 5, *n* = 115; U-Mann–Whitney, ***P = 0.0002). **(I)** sh*Luci* and sh*Pls3* growth cones unstimulated and 15 min BDNF stimulated stained against p-TrkB (gray) and F-actin (Phalloidin, yellow). Normalized mean gray values of p-TrkB (N = 3, *n* = 100; ANOVA Kruskal–Wallis, **P ≤ 0.01; ****P ≤ 0.0001). **(J)** sh*Luci* and sh*Pls3* growth cones stimulated and stained against surface TrkB (gray) and SYP (magenta). Normalized mean gray values of surface TrkB upon 15 min BDNF stimulation (N = 4, *n* = 90; ANOVA Kruskal–Wallis, ***P ≤ 0.001; ****P ≤ 0.0001) and 20 min 8-CPT-cAMP stimulation within axon terminals from sh*Luci* and sh*Pls3* motoneurons (N = 4, *n* = 95; ANOVA Kruskal–Wallis, **P ≤ 0.01; ****P ≤ 0.0001). **(K)** sh*Luci* and sh*Pls3* growth cones stained against $Ca_v2.2$ (gray) and F-actin (Phalloidin, yellow). Normalized mean gray values of $Ca_v2.2$ (N = 4, *n* = 100; U-Mann–Whitney, ****P ≤ 0.0001). **(L)** Maximum intensity projections of structured illumination microscopy (SIM) images of sh*Luci* and sh*Pls3* growth cones stained against $Ca_v2.2$ (cyan) and F-actin (Phalloidin, yellow). Arrows indicate "cluster-like" accumulations. **(M)** Representative plots of Cal-590 AM fluorescent changes over 1 min indicating spontaneous Ca^{2+} spikes of sh*Luci* and sh*Pls3* growth cones. Quantification of spontaneous Ca^{2+} spikes per minute (N = 5; *n* = 89; sh*Luci* 4.782 ± 0.4410 vs. sh*Pls3*: 1.483 ± 0.2137; U-Mann–Whitney, ****P ≤ 0.0001). Bar represent the mean ± SEM. Data are presented as scatter dot plot with bar. Bar represent the mean ± SEM (except for B). Scale bars: 5 µm.

as the activation of TrkB leading to enhanced BDNF/TrkB signaling.

Human PLS3 overexpression counteracts reduced $Ca_v2.2$ "cluster-like" formations and spontaneous Ca^{2+} transients in Smn-deficient motoneurons

Based on our previous results on TrkB and the fact that Pls3 knockdown interferes with $Ca_v2.2$ localization and function, we examined whether hPLS3 overexpression can rescue disturbed $Ca_v2.2$ "cluster-like" formations in SMA motoneurons (Jablonka et al., 2007). As shown before (Jablonka et al., 2007), $Ca_v2.2$ immunoreactivity was significantly reduced in LV-*mCh* transduced Smn-deficient neurons (Fig. 7 A). Intriguingly, hPLS3 overexpression improved the levels of $Ca_v2.2$ in these terminals (Fig. 7 A). Furthermore, we used SIM to test whether the "cluster-like" accumulations of these VGCCs is restored as well. Indeed, comparison of "cluster-like" $Ca_v2.2$ structures revealed less of these accumulations in SMA motoneurons transduced with LV-*mCh*, while multiple of these structures could be observed in hPLS3-overexpressing SMA motoneurons (Fig. 7 B). Next, we examined the functionality of the VGCCs using the calcium imaging technique. LV-*mCh* transduced Smn-deficient motoneurons showed significantly reduced frequencies of spontaneous spike-like Ca^{2+} transients (Fig. 7 C) in comparison with control motoneurons. In contrast, overexpression of hPLS3 markedly increased the frequency of spike-like spontaneous Ca^{2+} transients in the axon terminals of SMA motoneurons to normal levels observed in control motoneurons (Fig. 7 C). Hence, hPLS3 overexpression in SMA motoneurons improves "cluster-like" formations of $Ca_v2.2$ and enhances frequency of spontaneous Ca^{2+} transients.

Overexpression of hPLS3 rescues defective TrkB cell surface translocation after BDNF stimulation

In SMA motoneurons, basal levels of surface TrkB and endocytosis after BDNF stimulation seems to be unchanged. However, the cAMP-mediated membrane translocation is highly impaired upon Smn deficiency. Therefore, the question arises why the raise of p-TrkB after a 15 min BDNF stimulation is abolished in Smn-deficient axon terminals compared to controls. A possible mechanism that could explain the failure in TrkB activation is based on the self-amplifying actions of BDNF, since it was shown to be capable of triggering TrkB surface insertion for signal amplification (Cheng et al., 2011). Thus, BDNF stimulation leads to activation and internalization of TrkB, but could also promote in a positive feedback loop further recruitment of TrkB to the plasma membrane (Andreska et al., 2020; Cheng et al., 2011). Based on our observations that CytoD treatment abolished cAMP-mediated TrkB translocation to the cell surface (Fig. 2 C), the TrkB recruitment is dependent on a proper working actin cytoskeleton. Thus, the self-amplifying mechanism by local enhancement of available TrkB that is activated by BDNF stimulation seems to be impaired in SMA motoneurons, which would explain the decreased p-TrkB levels. To test this hypothesis, we investigated re-constitution of cell surface TrkB levels after BDNF stimulation. Control and Smn-deficient motoneurons were stimulated with BDNF for 5 min, then BDNF-containing medium was washed out, and the neurons were allowed to recover for 10 min. The comparison of TrkB surface levels showed that upon 5 min BDNF stimulation, the receptors disappeared from the cell surface (Fig. 8 A) as shown before (Fig. 2 A). However, following a 10 min recovery phase, the levels of TrkB at the cell surface started to reconstitute in axon terminals of control cells (Fig. 8 A). Thus, this assay reveals that more TrkB is re-located to the cell surface after BDNF-induced endocytosis of the receptor. In SMA growth cones, the recruitment of TrkB to the cell surface during the recovery phase failed (Fig. 8 A). To confirm that this process is dependent on a functional actin cytoskeleton, control motoneurons were treated with CytoD, Nocodazole (which blocks microtubule polymerization), or Cycloheximide (which interferes with protein synthesis) prior to the 10 min recovery assay. CytoD pre-treatment prevented the reconstitution of TrkB to the cell surface during the 10 min recovery phase, while disrupting the microtubules with Nocodazole had only minor effects (Fig. 8 B). Moreover, these data show that the receptors are recruited from an already existing intracellular pool rather than being newly synthetized, since protein translational elongation blockage by Cycloheximide had no

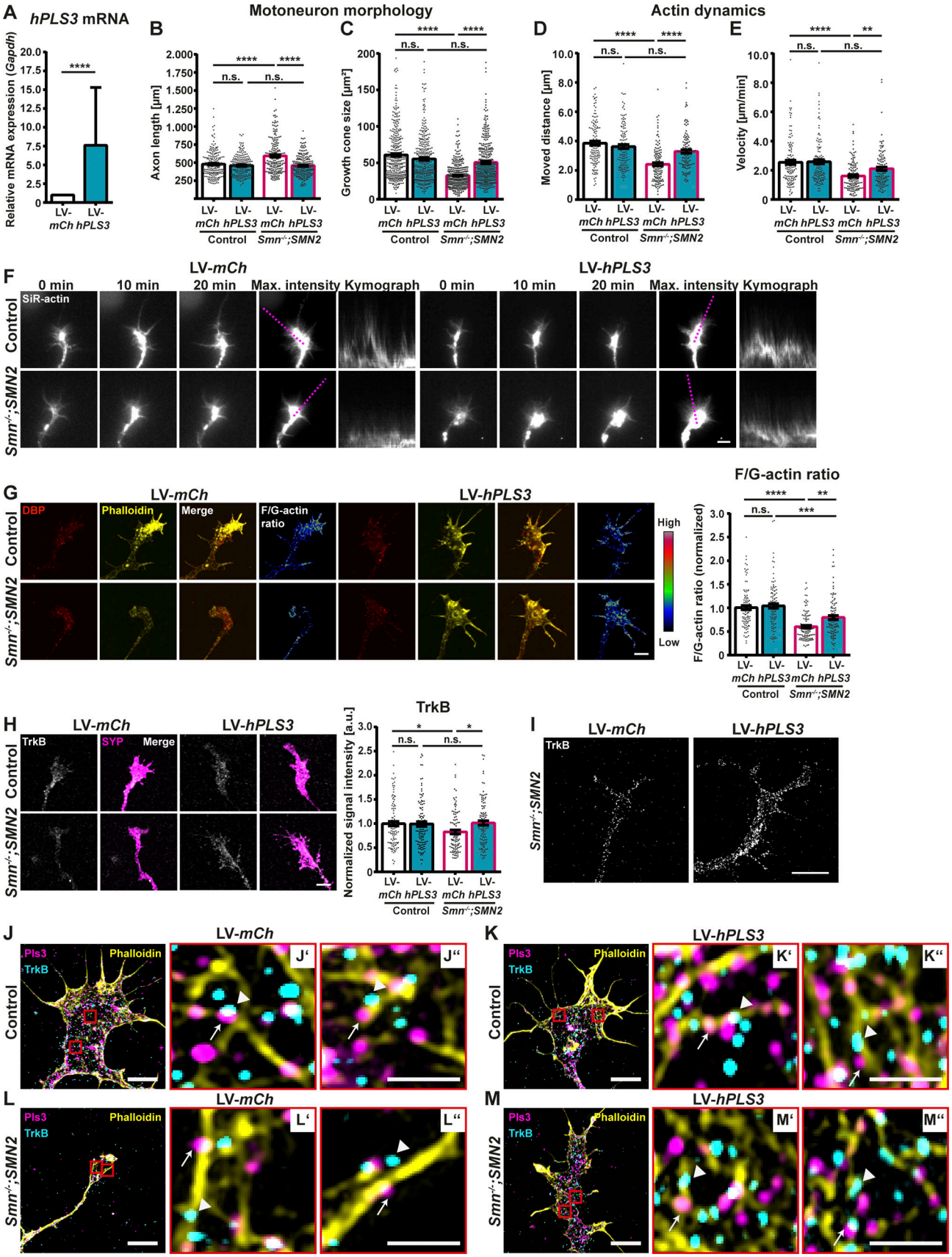

Figure 5. **Overexpression of hPLS3 normalizes growth cones morphology, actin dynamics and TrkB translocation in Smn-deficient motoneurons.** **(A)** Relative expression of *hPLS3* in whole-cell lysates of LV-*mCh* and LV-*hPLS3* transduced control motoneurons. Quantification of *hPLS3* relative to *Gapdh* (N =

6, *n* = 10; U-Mann–Whitney, ****P ≤ 0.0001). Data are presented as mean ± SD. **(B and C)** hPLS3 overexpression in *Smn*$^{-/-}$;*SMN2* motoneurons results in (B) rescued axon lengths (N = 3; *n* = 200; control LV-*mCh*: 478.8 ± 12.5 µm, control LV-*hPLS3*: 460.1 ± 9.8 µm, *Smn*$^{-/-}$;*SMN2* LV-*mCh*: 593.7 ± 17.1 µm, *Smn*$^{-/-}$;*SMN2* LV-*hPLS3*: 459.1 ± 10.2 µm; ANOVA Kruskal–Wallis, ****P ≤ 0.0001) and (C) increased growth cone sizes (N = 6; *n* = 350; control LV-*mCh*: 60.74 ± 1.85 µm^2, control LV-*hPLS3*: 55.24 ± 1.73 µm^2, *Smn*$^{-/-}$;*SMN2* LV-*mCh*: 32.38 ± 0.91 µm^2, *Smn*$^{-/-}$;*SMN2* LV-*hPLS3*: 50.30 ± 1.58 µm^2; ANOVA Kruskal–Wallis, ****P ≤ 0.0001). **(D–F)** LV-*mCh* and LV-*hPLS3* transduced control and *Smn*$^{-/-}$;*SMN2* growth cones with SiR-actin were monitored for 20 min. ROI (purple dotted line) of a single filopodia with the corresponding kymograph. **(D)** Quantification of the moved distance (amplitude in µm; N = 3; *n* = 122; ANOVA Kruskal–Wallis, ****P ≤ 0.0001) and (E) of the velocity (distance [µm] over time [min]) of single filopodia in LV-*mCh* and LV-*hPLS3* transduced control and *Smn*$^{-/-}$;*SMN2* growth cones (N = 3; *n* = 123; ANOVA Kruskal–Wallis, **P ≤ 0.01; ****P ≤ 0.0001). **(G)** LV-*mCh* and LV-*hPLS3* transduced control and *Smn*$^{-/-}$;*SMN2* growth cones stained against F-actin (Phalloidin, yellow) and G-actin (through Vitamin D-binding protein [DBP], red). Ratiometric images were generated by dividing F-actin by G-actin. Normalized F/G-actin ratio (N = 4, *n* = 102; ANOVA Kruskal–Wallis, **P ≤ 0.01; ***P ≤ 0.001; ****P ≤ 0.0001). **(H)** LV-*mCh* and LV-*hPLS3* transduced control and *Smn*$^{-/-}$;*SMN2* growth cones stained against TrkB (gray) and Synaptophysin-1 (SYP, magenta), Normalized mean gray values of TrkB (N = 4, *n* = 105; ANOVA Kruskal–Wallis, *P ≤ 0.05). **(I)** Maximum intensity projections of SIM images of control and *Smn*$^{-/-}$;*SMN2* growth cones transduced with LV-*mCh* and LV-*hPLS3* stained against TrkB (gray). **(J–M)** Maximum intensity projections of SIM images of control and *Smn*$^{-/-}$;*SMN2* growth cones transduced with LV-*mCh* and LV-*hPLS3* stained against Pls3 (magenta), TrkB (cyan), and F-actin (Phalloidin, yellow). Red boxes indicated ROIs of the zoomed images represented as ′ and ″. **(J′–M′ and J″–M″)** Detailed zoomed-in images of J–M. Arrows indicate Pls3, and arrowheads indicate TrkB along actin filaments. Scale bar: 1 µm. Data are presented as scatter dot plot with bar. Bar represents the mean ± SEM (except for A). Scale bars: 5 µm (except for J′–M′ and J″–M″).

effect on the recovery (Fig. 8 B). This was further confirmed by a Pls3 knockdown in wild-type motoneurons. Depletion of Pls3 prevented the reconstitution of surface TrkB levels during the recovery phase (Fig. 8 C) in a similar manner as in Smn-deficient motoneurons. In line with this, hPLS3 overexpression in SMA motoneurons showed a strong rescue of the defects in TrkB translocation to the cell surface (Fig. 8 D). Next, we asked whether the rapid recovery of surface TrkB is based on recycled receptors that had been on the surface prior to BDNF stimulation, or whether they originate from the intracellular pool of TrkB. For this purpose, we performed a TrkB recycling assay on living motoneurons (Fig. 8 E; see Materials and methods). Motoneurons were exposed to a TrkB antibody and secondary antibody prior to BDNF stimulation, and a second TrkB staining was performed after the recovery phase to directly follow TrkB fate within individual growth cones (Fig. 8 E). While in control motoneurons the baseline levels of TrkB are reconstituted up to ∼67%, only ∼40% of TrkB are detectable at the cell surface upon recovery in Smn-deficient motoneurons. Improving the actin dynamics by hPLS3 overexpression rescued the recovery in SMA axon terminals (∼72%) to control level (Fig. 8 F). Interestingly, we observed that approximately half of the recovered TrkB have previously been at the surface in control motoneurons (57.7%) as well as in Smn-deficient cells (55.8%). Thus, this assay shows that the highly impaired TrkB recovery in SMA motoneurons is due to an actin-dependent translocation defect to the cell surface rather than disturbed surface TrkB recycling per se.

In conclusion, our data support the hypothesis that TrkB is rapidly translocated to the plasma membrane after ligand-induced internalization and that this process depends on an intact actin cytoskeleton.

Pls3 and Arp2/3 cooperate for proper surface translocation of intracellular proteins

To gain further insights into the role of PLS3 in promoting F-actin-mediated surface translocation of transmembrane proteins, we examined the interaction with additional actin-modulating factors. One candidate is the actin-related protein 2/3 (Arp2/3) complex, which was recently shown to be markedly diminished at the leading edge of endothelial cells upon loss of PLS3 (Garbett et al., 2020). Furthermore, transcripts encoding for the complex components Arpc1b and Arpc4 appeared to be downregulated in the axonal compartment of Smn knockdown motoneurons (Fig. 3 G). Arp2/3 is an actin-nucleator that initiates the formation of branched actin filaments (Lee et al., 2010; Suraneni et al., 2012; Welch et al., 1997; Wu et al., 2012a), which are primarily bundled by PLS3 (Skau et al., 2011). We first checked the levels of the Arp2/3 complex in the growth cones of control and Smn-deficient motoneurons with an Arp3 antibody. Interestingly, the expression of Arp3 was reduced within axon terminals of SMA motoneurons (Fig. 9 A). SIM images revealed that Pls3 is distributed all over the growth cone but is highly enriched within F-actin-rich protrusions, while Arp3 is mainly located in the core of the growth cone (Fig. 9 B). The expression of Arp3 was also significantly reduced in growth cones upon knockdown of Pls3 in wild-type motoneurons (Fig. 9 C). In turn, overexpression of hPLS3 in Smn-deficient motoneurons resulted in restoration of the Arp3 signal to control level (Fig. 9 D). To better understand the relationship of Arp2/3-mediated actin-branching and TrkB membrane translocation, we pre-treated motoneurons with the Arp2/3 inhibitor CK-666 and used our live-cell staining protocol. Intriguingly, addition of CK-666 before and during BDNF stimulation and recovery phase prevented the recruitment of TrkB in control motoneurons, while no further effect was observed in SMA motoneurons (Fig. 9 E). Next, we wanted to figure out whether the beneficial effects of hPLS3 overexpression on translocation of TrkB upon BDNF stimulation are abolished by Arp2/3 inhibition. Indeed, we found that CK-666 treatment abolished the rescuing effect of hPLS3 overexpression in Smn-deficient motoneurons. No TrkB recruitment to the cell surface was detectable anymore upon recovery (Fig. 9 F). Altogether, these results indicate that a well-balanced cooperation of the Arp2/3 complex and Pls3 is required for the function of the actin cytoskeleton in mediating the ligand-induced translocation of TrkB to the cell surface. In addition to the members of the Arp2/3 complex *Arpc4* and *Arpc1b*, RNA-seq analysis revealed the downregulation of *Pfn1* transcripts in the axonal compartment of Smn knockdown motoneurons (Fig. 3 F). Profilin inherits complex functions and is involved in the regulation of directed actin polymerization (Hensel and Claus, 2018; Witke, 2004). Moreover, is has been shown that altered profilin

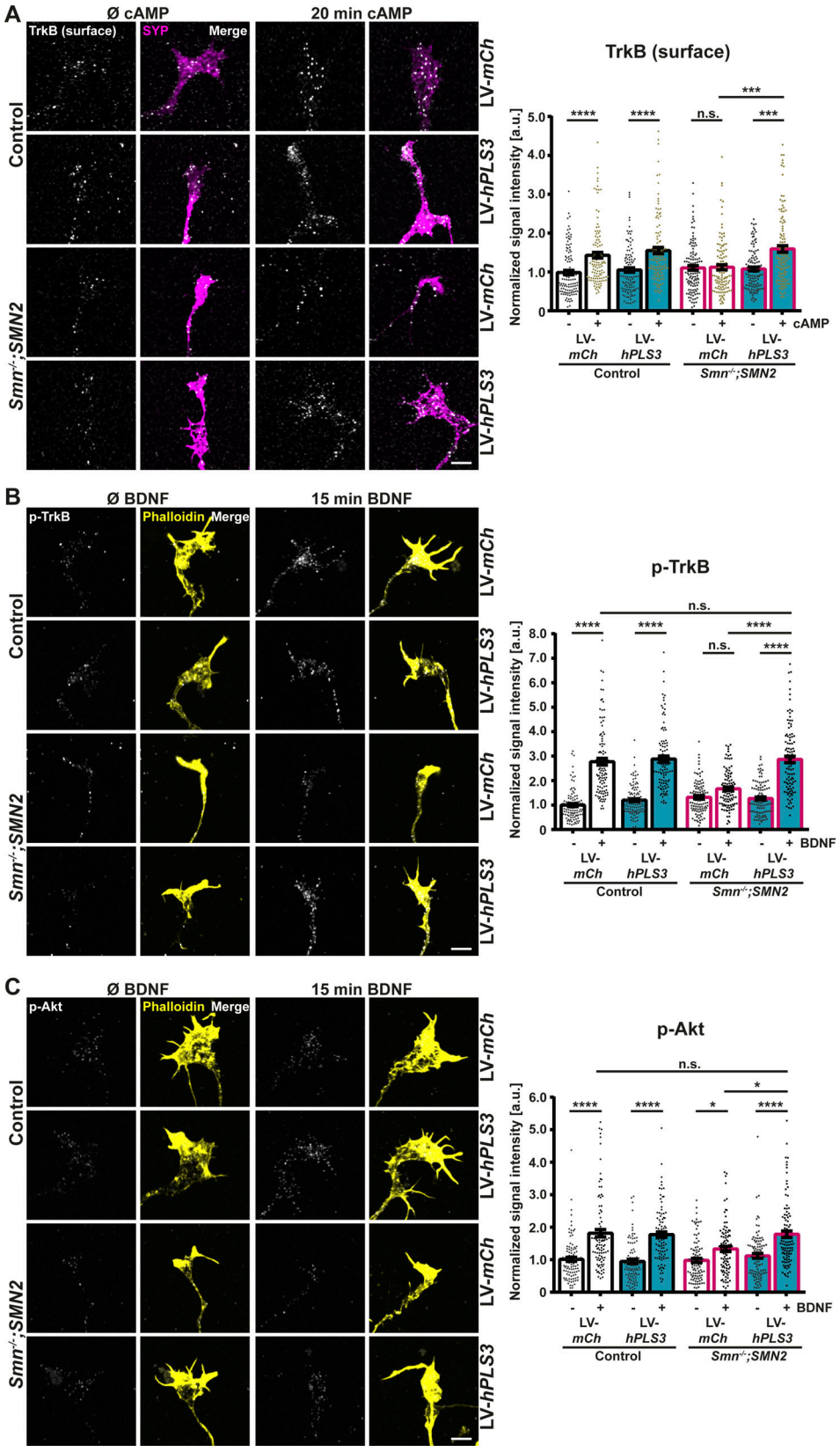

Figure 6. **Overexpression of hPLS3 restores TrkB phosphorylation and Akt phosphorylation in Smn-deficient motor axon terminals. (A)** LV-*mCh* and LV-*hPLS3* transduced control and *Smn*$^{-/-}$;*SMN2* growth cones unstimulated and 20 min 8-CPT-cAMP stimulated stained against surface TrkB (gray) and Synaptophysin-1 (SYP, magenta). Normalized mean gray values of surface TrkB (N = 4, *n* = 115; ANOVA Kruskal–Wallis, ***P ≤ 0.001; ****P ≤ 0.0001). **(B and C)** Unstimulated or 15 min BDNF stimulated growth cones from control and *Smn*$^{-/-}$;*SMN2* motoneurons transduced with LV-*mCh* and LV-*hPLS3* stained against (B) p-TrkB (gray) or (C) p-Akt (gray) and F-actin (Phalloidin, yellow). (B) Normalized mean gray values of p-TrkB in LV-*mCh* or LV-*hPLS3* transduced

control and *Smn*$^{-/-}$;*SMN2* terminals (N = 4, *n* = 105; ANOVA Kruskal–Wallis, ****P ≤ 0.0001). **(C)** Normalized mean gray values of p-Akt in LV-*mCh* or LV-*hPLS3* transduced control and *Smn*$^{-/-}$;*SMN2* terminals (N = 4, *n* = 98; ANOVA Kruskal–Wallis, *P ≤ 0.05; ****P ≤ 0.0001). Data are presented as scatter dot plot with bar. Bar represents the mean ± SEM. Scale bars: 5 µm.

protein levels could be involved in the pathogenesis of SMA (Antoine et al., 2020; Bowerman et al., 2007). Hence, we examined whether overexpression of hPLS3 beneficially acts on the regulation of profilin. Therefore, we quantified levels of profilin using a pan-profilin antibody in motor axon terminals. SMA motoneurons transduced with LV-*mCh* displayed significantly decreased levels of profilin immunoreactivity, which were significantly enhanced upon overexpression of hPLS3 (Fig. S3 A). Since the activity of profilin is regulated by phosphorylation, we also tested the phosphorylation status of profilin (p-profilin). Under standard conditions, no alterations in p-profilin levels were observed in SMA axon terminals (Fig. S3 B). Recently, profilin phosphorylation was shown to be stimulated by BDNF (Dombert et al., 2017). Therefore, motoneurons were exposed to BDNF for 15 min, and the p-profilin levels were examined. In control motoneurons transduced with LV-*mCh* or LV-*hPLS3*, a

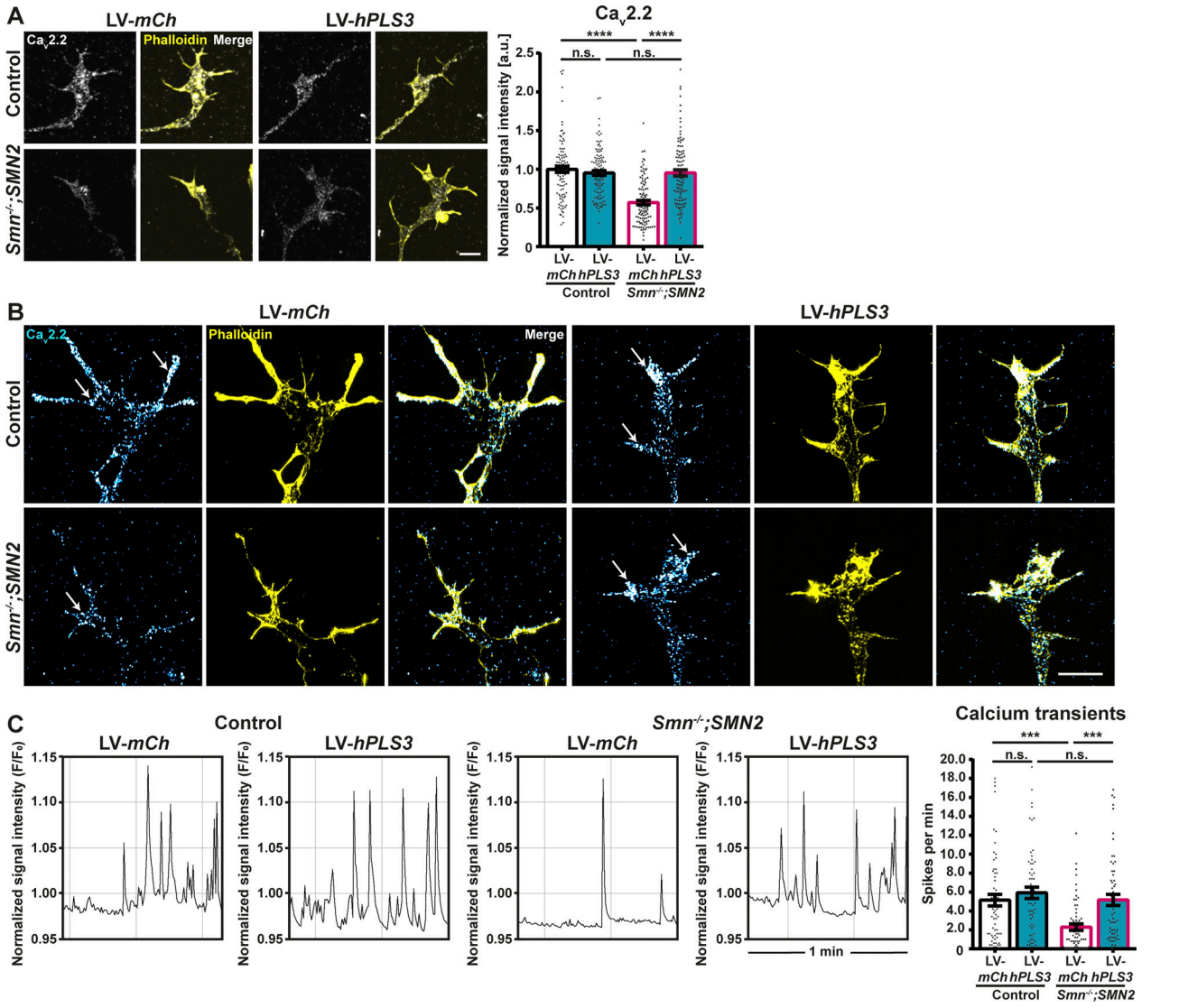

Figure 7. **Overexpression of hPLS3 restores $Ca_v2.2$ "cluster-like" formations and spontaneous Ca^{2+} transients in Smn-deficient growth cones. (A)** LV-*mCh* and LV-*hPLS3* transduced control and *Smn*$^{-/-}$;*SMN2* growth cones stained against $Ca_v2.2$ (gray) and F-actin (Phalloidin, yellow). Normalized mean gray values of $Ca_v2.2$ (N = 5, *n* = 105; ANOVA Kruskal–Wallis, ****P ≤ 0.0001). **(B)** Maximum intensity projections of SIM images of LV-*mCh* and LV-*hPLS3* transduced control and *Smn*$^{-/-}$;*SMN2* growth cones stained against $Ca_v2.2$ (cyan) and F-actin (Phalloidin, yellow). Arrows indicate "cluster-like" accumulations. **(C)** Representative plots of Oregon Green 488 BAPTA-1 fluorescent changes over 5 min indicating spontaneous Ca^{2+} spikes of control and *Smn*$^{-/-}$;*SMN2* motoneurons transduced with LV-*mCh* and LV-*hPLS3*. Quantification of spontaneous Ca^{2+} spikes per minute (N = 4; *n* = 60; control LV-*mCh*: 5.140 ± 0.6073, control LV-*hPLS3*: 5.910 ± 0.5955, *Smn*$^{-/-}$;*SMN2* LV-*mCh*: 2.293 ± 0.3466, *Smn*$^{-/-}$;*SMN2* LV-*hPLS3*: 5.163 ± 0.5820; ANOVA Kruskal–Wallis, ***P ≤ 0.001). Bar represents the mean ± SEM. Scale bars: 5 µm.

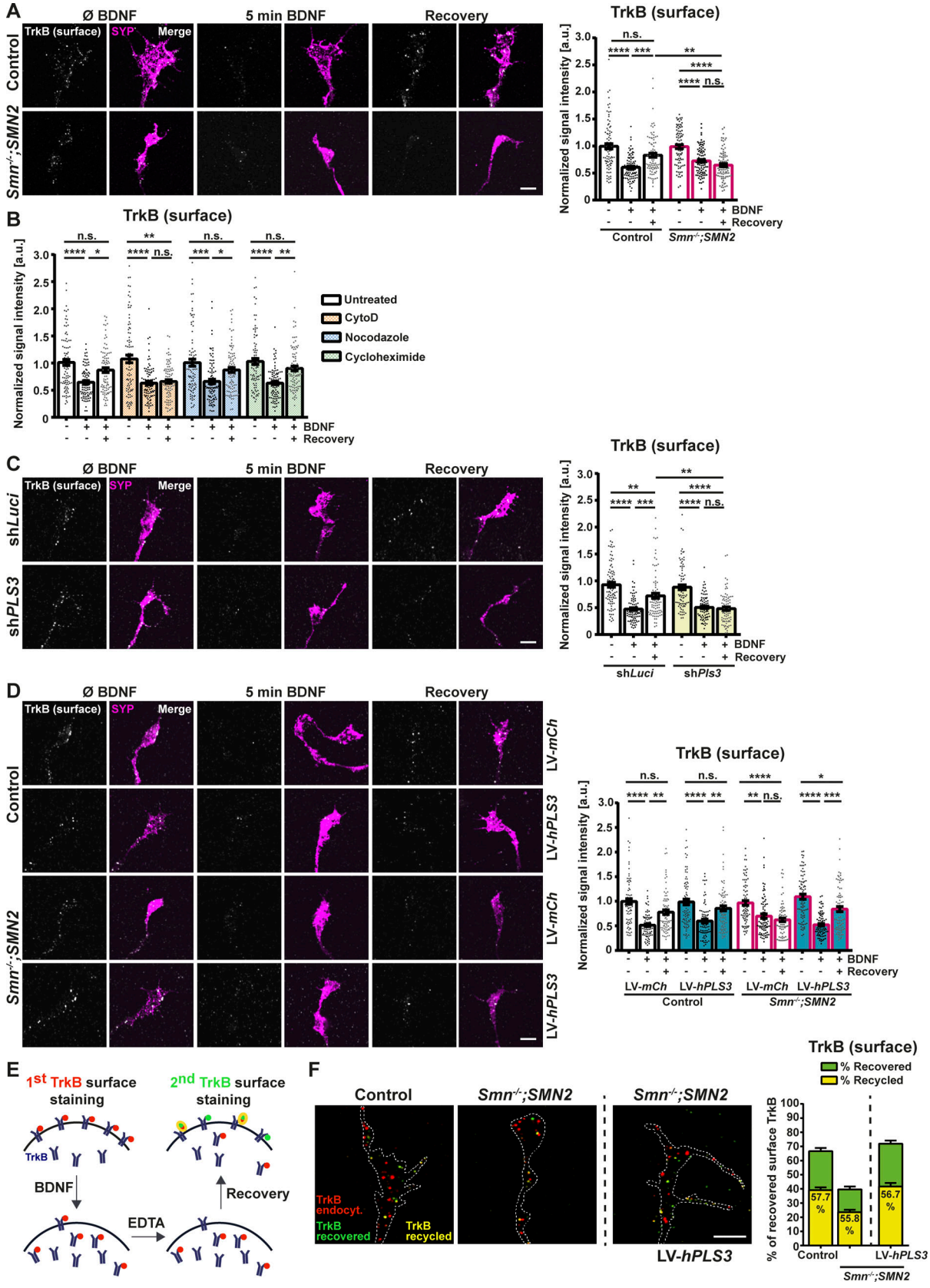

Figure 8. **Overexpression of hPLS3 corrects TrkB surface translocation after BDNF stimulation in Smn-deficient motoneurons. (A)** Control and *Smn*$^{-/-}$;*SMN2* growth cones unstimulated, 5 min BDNF stimulated and 5 min BDNF stimulated followed by a 10 min recovery phase (recovery assay) stained against surface TrkB (gray) and Synaptophysin-1 (SYP, magenta). Normalized mean gray values of surface TrkB (N = 3, *n* = 90; ANOVA Kruskal–Wallis,

P ≤ 0.01; ***P ≤ 0.001; ****P ≤ 0.0001). **(B) Normalized mean gray values of surface TrkB in axon terminals of control motoneurons that were treated with 0.5 µM Cytochalasin D (CytoD), 10 µM Nocodazole and 20 µM Cycloheximide prior to the recovery assay (N = 4, *n* = 90; ANOVA Kruskal–Wallis, *P ≤ 0.05; **P ≤ 0.01; ***P ≤ 0.001; ****P ≤ 0.0001). **(C)** sh*Luci* and sh*Pls3* growth cones subjected to the recovery assay and stained against surface TrkB (gray) and SYP (magenta). Normalized mean gray values of surface TrkB (N = 3, *n* = 85; ANOVA Kruskal–Wallis, **P ≤ 0.01; ***P ≤ 0.001; ****P ≤ 0.0001). **(D)** LV-*mCh* and LV-*hPLS3* transduced control and *Smn*$^{-/-}$;*SMN2* growth cones were subjected to the recovery assay and stained against surface TrkB (gray) and SYP (magenta). Normalized mean gray values of surface TrkB (N = 3, *n* = 80; ANOVA Kruskal–Wallis, *P ≤ 0.05; **P ≤ 0.01; ***P ≤ 0.001; ****P ≤ 0.0001). **(E)** Schematic of the TrkB recycling assay. For details, see Materials and methods section. **(F)** Growth cones of control and *Smn*$^{-/-}$;*SMN2*; as well as LV-*hPLS3*-*Smn*$^{-/-}$;*SMN2* motoneurons stained against surface TrkB (red = receptors that have been on the cell surface prior to BDNF stimulation, green = receptors located at the cell surface after recovery, yellow = co-localizing). Quantification (N = 3, *n* = 98) of (green), the number of recovered receptors (percentage of total TrkB) and (yellow) the number of recycled receptors (percentage of recovered TrkB). Data are presented as scatter dot plot with bar/bar. Bar represents the mean ± SEM. Scale bars: 5 µm.

marked increase in p-profilin quantities was detected upon BDNF stimulation (Fig. S3 B). In contrast to that, no such increase was measurable in LV-mCh transduced Smn-deficient motoneurons. Again, when hPLS3 was overexpressed, the BDNF-induced profilin phosphorylation was normalized to control levels (Fig. S3 B). In contrast to that, the levels of cofilin (Fig. S3 C), an actin-depolarization factor (Sarmiere and Bamburg, 2004), or myosin VI, which acts in a complex with TrkB for the retrograde signaling (Yano et al., 2006a), were not altered in SMA motoneurons (Fig. S3 D).

In vivo hPLS3 overexpression ameliorates BDNF-induced TrkB activation and improves the neuromuscular phenotype in *SMNΔ7* mice

In order to investigate the effect of hPLS3 on stabilizing the actin cytoskeleton in motor nerve terminals in vivo, we overexpressed hPLS3 through adeno-associated viruses 9 (AAV9). *SMNΔ7* mice were injected with AAV9-*hPLS3* or AAV9-*EGFP* at P0/P1, and the NMJs of the animals were analyzed at the later-symptomatic stage P10-P11. Overexpression of hPLS3 was verified in motoneurons through HA-tag within the spinal lumbar L1 segment (Fig. S4). Morphological investigations revealed an increased ratio of occupancy of postsynaptic areas by presynaptic terminals upon hPLS3 overexpression in Smn-deficient NMJs (Fig. 10 A). Examination of the amount of G-actin within the presynaptic terminals showed significantly lower levels in Smn-deficient endplates, while overexpression of hPLS3 elevated the level of G-actin (Fig. 10 B). In addition, total TrkB levels within the presynapse increased upon overexpression of hPLS3 in axon terminals of *SMNΔ7* mice (Fig. 10 C). To test whether overexpression of hPLS3 manifests in considerable improvements of TrkB signaling at the NMJ, TVA muscle explants were stimulated with BDNF, and the activation of TrkB was measured in the axon terminals. Strikingly, and in contrast to the AAV9-*EGFP*-injected *SMNΔ7* mice, AAV9-*hPLS3*-treated SMA pups showed a marked increase in p-TrkB immunosignal in the NMJs upon BDNF stimulation (Fig. 10 D). Thus, hPLS3 overexpression exhibits a favorable effect on TrkB localization and ligand-induced activation in Smn-deficient NMJs.

Moreover, $Ca_v2.1$ "cluster-like" formations were decreased in the neuromuscular endplate of AAV9-*EGFP*-injected *SMNΔ7* mice, which was significantly improved when hPLS3 was overexpressed in these animals (Fig. 10 E). Hence, our in vivo data demonstrate that postnatal overexpression of hPLS3 in a severe SMA mouse model has beneficial effects on the activation of TrkB and partially improves the progressive NMJ deterioration.

Discussion

Given the tremendous impact of BDNF/TrkB signaling on neuronal survival and differentiation (Kowiański et al., 2018), it is not surprising that dysregulations of this mechanism play a crucial role in various diseases such as Alzheimer's disease (Amidfar et al., 2020), Parkinson's disease (Palasz et al., 2020), or epilepsy (Lin et al., 2020). However, the underlying mechanisms vary strongly between different diseases, reaching from neuroprotective to neurotoxic effects, as recently reported for amyotrophic lateral sclerosis (ALS; Pradhan et al., 2019). This makes it challenging to develop approaches for alternative therapeutic strategies based on BDNF/TrkB signaling. Focusing on SMA, we aimed to decipher the cellular mechanisms that underlie altered TrkB cell surface exposure and impaired BDNF-induced activation and signaling. Our study provides evidence that TrkB phosphorylation and downstream signaling such as Akt phosphorylation after BDNF stimulation is reduced in Smn-deficient growth cones, although TrkB presentation at the cell surface under basal conditions is unaltered. In SMA axon terminals, BDNF-mediated TrkB endocytosis is working properly in contrast to the activity-mediated TrkB recruitment to the plasma membrane and its re-translocation upon BDNF-mediated activation. The fact that the levels of myosin VI, which was shown to be responsible for the retrograde transport of BDNF/TrkB signaling endosomes (Yano et al., 2006a), were unaltered in SMA motoneurons further indicates that BDNF/TrkB complex endocytosis is functioning in SMA axon terminals. However, TrkB recycling experiments revealed that baseline TrkB levels are reconstituted after BDNF stimulation up to ∼67% in control cells, while in Smn-deficient motoneuron terminals only ∼40% of baseline TrkB level are observed upon recovery. We concluded that a self-amplifying mechanism of BDNF by locally enhancing the amount of available TrkB at the cell surface for signal amplification corresponds to proper F-actin assembly that is dysfunctional in SMA motor axon terminals. Based on this assumption, we started focusing on PLS3 and its connection to the F-actin cytoskeleton. Although PLS3 has been already shown to beneficially modify the severity of the SMA phenotype in patients and relevant animal models (Ackermann et al., 2013; Alrafiah et al., 2018; Dimitriadi et al., 2010; Hao et al., 2012; Hosseinibarkooie et al., 2016; Lyon et al., 2013; Oprea et al.,

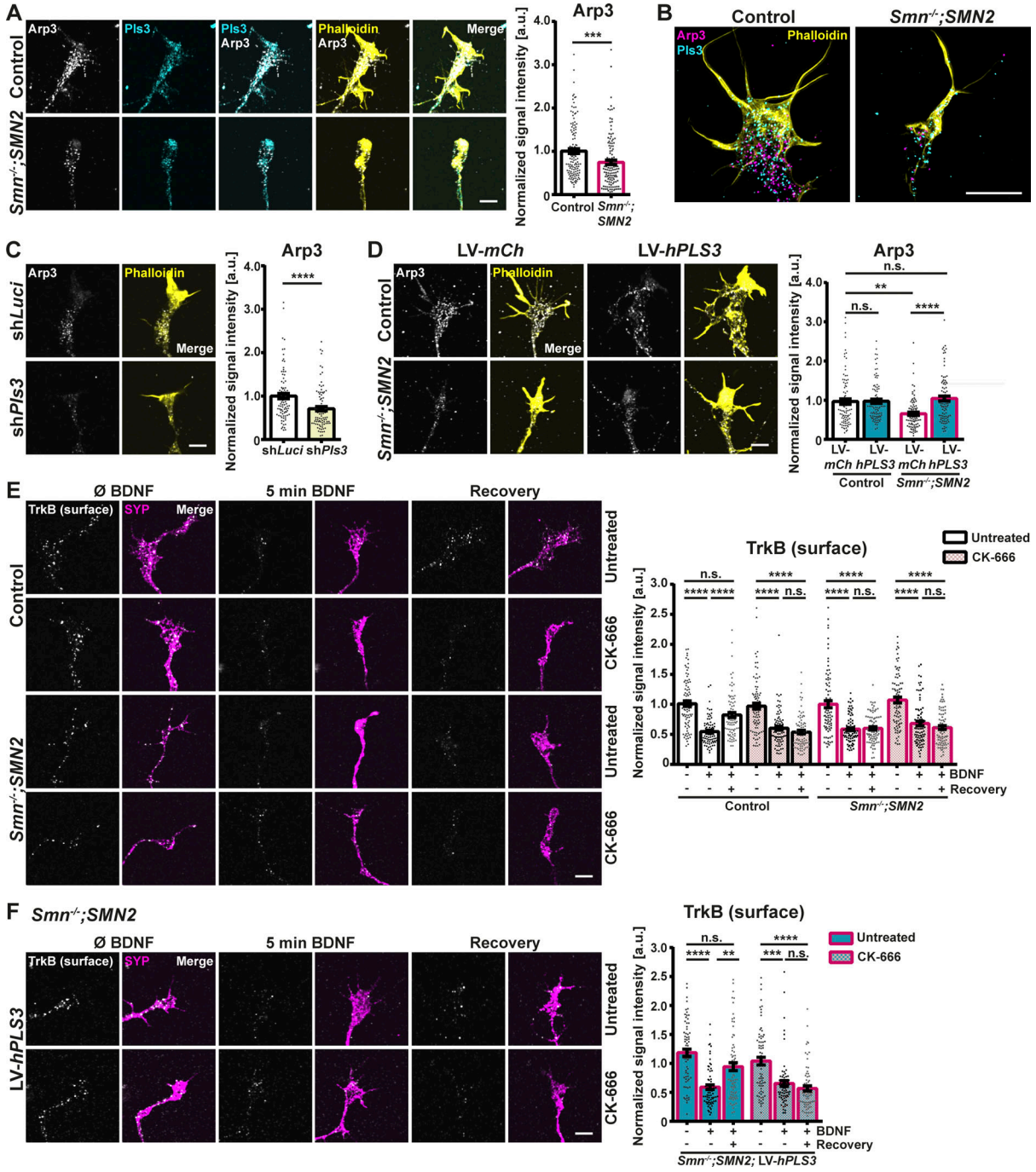

Figure 9. **Arp2/3 and Pls3 are required for the correct translocation of TrkB to the cell surface. (A)** Control and *Smn*$^{-/-}$;*SMN2* growth cones stained against Arp3 (gray), Pls3 (cyan) and F-actin (Phalloidin, yellow). Normalized mean gray values of Arp3 (N = 4, *n* = 130; U-Mann–Whitney, ***P ≤ 0.001). **(B)** Maximum intensity projections of SIM images of control and *Smn*$^{-/-}$;*SMN2* growth cones stained against Arp3 (magenta), Pls3 (cyan) and F-actin (Phalloidin, yellow). **(C)** sh*Luci* and sh*Pls3* growth cones stained against Arp3 (gray) and F-actin (Phalloidin, yellow). Normalized mean gray values of Arp3 (N = 3, *n* = 90; U-Mann–Whitney, P **** ≤ 0.0001). **(D)** Growth cones from control and *Smn*$^{-/-}$;*SMN2* motoneurons transduced with LV-*mCh* and LV-*hPLS3* stained against Arp3 (gray) and F-actin (Phalloidin, yellow). Normalized mean gray values of Arp3 (N = 3, *n* = 90; ANOVA Kruskal–Wallis, P ** ≤ 0.01; P **** ≤ 0.0001). **(E)** Growth cones from control and *Smn*$^{-/-}$;*SMN2* motoneurons that were pre-treated with 50 µM CK-666 and stained against surface TrkB (gray) and Synaptophysin-1 (SYP, magenta). Normalized mean gray values of surface TrkB in control and *Smn*$^{-/-}$;*SMN2* terminals pre-treated with CK-666 and subjected to the recovery assay (N = 4, *n* = 83; ANOVA Kruskal–Wallis, ****P ≤ 0.0001). **(F)** Growth cones from *Smn*$^{-/-}$;*SMN2* motoneurons transduced with LV-*hPLS3* that were pre-treated with CK-666 and stained against surface TrkB (gray) and SYP (magenta). Normalized mean gray values of surface TrkB in LV-*hPLS3* transduced *Smn*$^{-/-}$;*SMN2* terminals (LV-mCh data not shown) pre-treated with CK-666 and subjected to the recovery assay (N = 3, *n* = 72; ANOVA Kruskal–Wallis, **P ≤ 0.01; ***P ≤ 0.001; ****P ≤ 0.0001). Data are presented as scatter dot plot with bar. Bar represents the mean ± SEM. Scale bars: 5 µm.

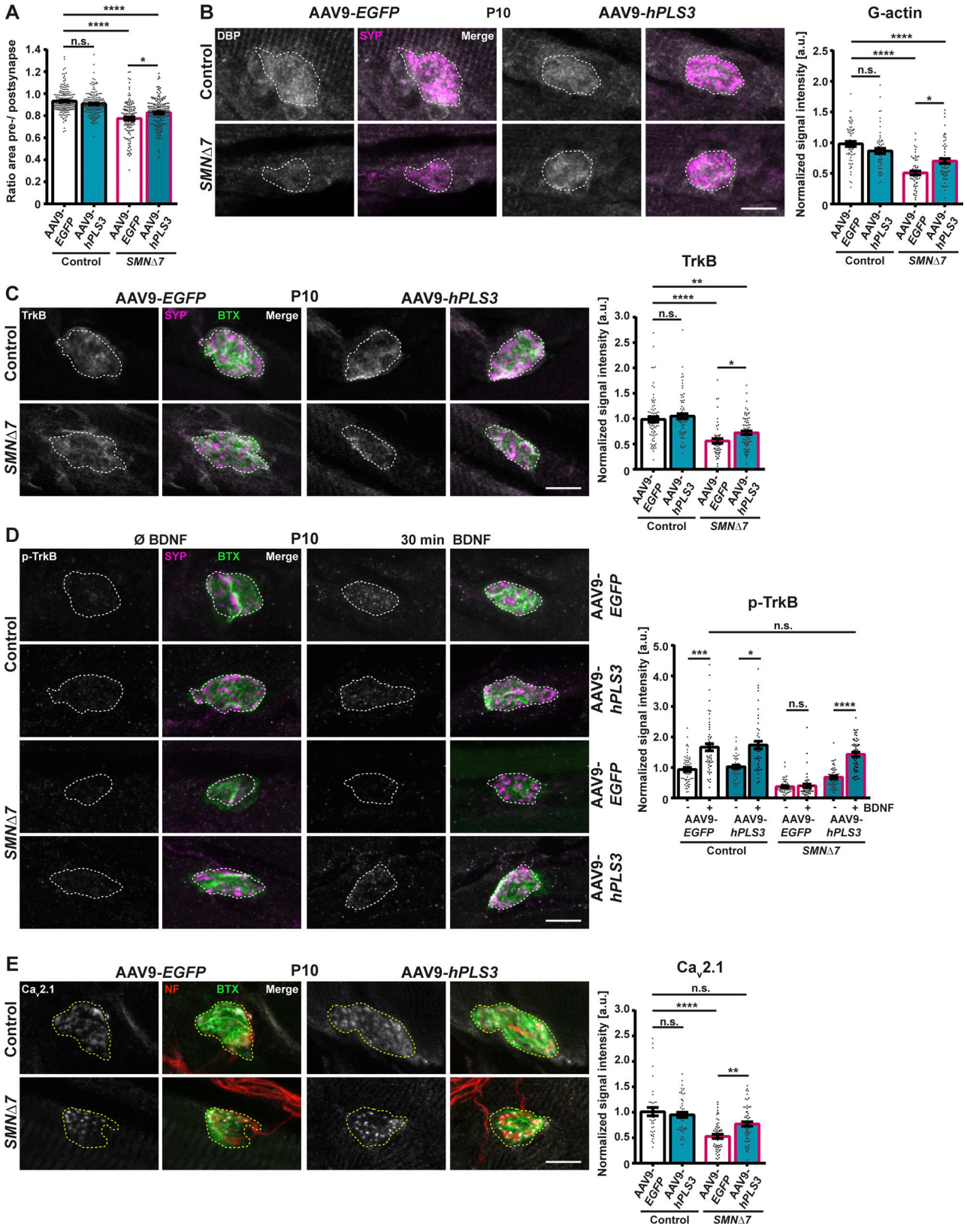

Figure 10. **In vivo hPLS3 overexpression improves TrkB phosphorylation and TrkB and Ca$_v$2.1 localization in NMJs of *SMNΔ7* mice. (A)** Ratio of the area of the presynapse (through Synaptophysin-1 [SYP]) vs. postsynapse (ACh receptors through Bungarotoxin [BTX]) of NMJs in the *Transversus abdominis anterior* (TVA) of control and *SMNΔ7* P10-P11 animals that were injected with AAV9-*EGFP* and AAV9-*hPLS3* (N = 10/10/5/7, *n* = 185/185/130/185; ANOVA Kruskal–Wallis, *P ≤ 0.05; ****P ≤ 0.0001). **(B)** NMJs in the TVA muscle of control and *SMNΔ7* P10 animals that were injected with AAV9-*EGFP* or AAV9-*hPLS3* stained against G-actin (through Vitamin D-binding protein [DBP], gray) and SYP (magenta). Dotted line depicts outline of the presynapse (SYP signal). Normalized

mean gray values of G-actin (N = 3/3/3/4, *n* = 60/60/60/60; ANOVA Kruskal–Wallis, *P ≤ 0.05; ****P ≤ 0.0001). **(C)** NMJs in the TVA muscle of control and *SMNΔ7* P10 animals that were injected with AAV9-*EGFP* or AAV9-*hPLS3* stained against TrkB (gray), SYP (magenta), and BTX (green). Dotted line depicts outline of the presynapse (SYP signal). Normalized mean gray values of TrkB (N = 5/5/3/4, *n* = 78/78/52/75; ANOVA Kruskal–Wallis, *P ≤ 0.05; **P ≤ 0.01; ****P ≤ 0.0001). **(D)** Unstimulated and 30 min BDNF stimulated NMJs in the TVA muscle of control and *SMNΔ7* P10 animals that were injected with AAV9-*EGFP* and AAV9-*hPLS3* and stained against p-TrkB (gray), SYP (magenta), and BTX (green). Dotted line depicts outline of the presynapse (SYP). Normalized mean gray values of p-TrkB (N = 6/4/3/3, *n* = 54/46/46/54; ANOVA Kruskal–Wallis, *P ≤ 0.05; ***P ≤ 0.001 ****P ≤ 0.0001). **(E)** NMJs in the TVA muscle of control and *SMNΔ7* P10 animals that were injected with AAV9-*EGFP* or AAV9-*hPLS3* stained against $Ca_v2.1$ (gray), neurofilament (NF, red), and BTX (green). Dotted yellow line depicts outline of the postsynapse (BTX signal). Normalized mean gray values of $Ca_v2.1$ (N = 3/4/3/4, *n* = 40/50/54/62; ANOVA Kruskal–Wallis, **P ≤ 0.01; ****P ≤ 0.0001). Data are presented as scatter dot plot with bar. Bar represents the mean ± SEM. Scale bars: 10 µm.

2008), the knowledge of the cellular mechanism behind the PLS3-compensatory effect is still fragmented, as recently reviewed (Wolff et al., 2021).

In our study, we could show that *Pls3* mRNA is downregulated together with other actin-related transcripts in the axonal compartment of Smn-deficient motoneurons. This underlines our hypothesis that reduced axon elongation of SMA motoneurons involves defects in the F-actin cytoskeleton (Jablonka et al., 2007; Rossoll et al., 2003; Rossoll et al., 2002). In the somatodendritic compartment, we observed a downregulation of transcripts associated with the microtubule cytoskeleton or GTPase activity that is indispensable for axonal transport. This could explain the disturbed membrane coverage of the rectifier channel $K_v2.1$ (Fletcher et al., 2017) that corresponds to impaired proprioceptive input on SMA somata (Fletcher et al., 2017; Mentis et al., 2011). The upregulation of transcripts whose corresponding proteins are involved in oxidative phosphorylation and ATP metabolism in both compartments of Smn-deficient motoneurons could represent a compensatory mechanism counteracting cytoskeletal defects. Beyond that, neuronal differentiation requires the switch from glycolysis to oxidative phosphorylation for enhanced ATP production (Iwata and Vanderhaeghen, 2021). Since SMA motoneurons show obvious mitochondrial dysregulations due to Ca^{2+} signaling alterations (Lopez-Manzaneda et al., 2021), the upregulation of those transcripts might compensate the mitochondrial dysfunctions and try to correct cellular differentiation.

The yet unanswered question about the cause of defective $Ca_v2.2$ cluster formations and reduced spontaneous Ca^{2+} transients in SMA motoneurons (Jablonka et al., 2007) seems to have found an answer. Pls3 is a crucial player in this scenario, as the Pls3 knockdown phenocopies the morphological and functional alterations of SMA motoneurons on the β2-chain laminin isoform (laminin-221/211). Beyond that, Pls3 knockdown also affects TrkB localization and phosphorylation that is newly reported in this study for SMA motoneurons. In addition, the importance of PLS3 is already reflected by its role as a genetic SMA modifier and could be confirmed by our rescue experiments with hPLS3 overexpression in Smn-deficient motoneurons. Overexpression of hPLS3 modulates F-actin dynamics and leads to improved cAMP-dependent recruitment of TrkB to the cell surface, as well as to reconstituted spontaneous Ca^{2+} transients based on improved $Ca_v2.2$ "cluster-like" formations in SMA axon terminals. Strikingly, this effect is comparable with previous observations on the beneficial effects of R-Roscovitine on SMA motoneurons. Application of this drug increases spontaneous Ca^{2+} transients by extending the open state of $Ca_v2.2$, leading to reconstituted cellular excitability and differentiation (Tejero et al., 2020). Similarly, chronic in vivo treatment of the K^+ channel blocker 4-aminopyridine, which increases neuronal activity and Ca^{2+} influx at presynaptic terminals, restores NMJ pathology through axonal sprouting in SMA mice (Simon et al., 2021).

Beyond this, the actin-bundling capacity of PLS3 is linked to the Arp2/3 actin nucleator complex (Giganti et al., 2005). Smn-deficient motoneurons are Arp3-reduced at their nerve terminals that significantly improved upon hPLS3 overexpression. More recently, Garbett and colleagues showed that PLS3 knockdown results in a defective protrusive network, including decreased levels of Arp3 and F-actin in lamellipodia (Garbett et al., 2020). In particular, the interplay between Pls3 and the Arp2/3 complex seems to be important for proper function of the actin cytoskeleton in motoneurons, as blockage of the Arp2/3 complex by CK-666 inhibited the rescuing effects of hPLS3 overexpression on TrkB translocation upon recovery. Besides Pls3 and Arp2/3, further regulatory proteins such as profilin or cofilin are required for proper functioning of the actin cytoskeleton. Profilin has specific functions in regulating the inclusion of G-actin to the barbed ends of F-actin (Hensel and Claus, 2018). Thus, it is not surprising that dysregulation of profilin is connected to the pathomechanism of motoneuron diseases such as ALS (Smith et al., 2015; Tanaka et al., 2016; Wu et al., 2012b) and SMA (Antoine et al., 2020; Bowerman et al., 2007; Giesemann et al., 1999). Moreover, in the context of SMA, a link between profilin levels and Pls3 has been already reported (Bowerman et al., 2009). In line with this, RNA-seq and immunocytochemistry revealed a reduction of profilin in SMA axon terminals. The baseline phosphorylation status of profilin was unaltered in SMA growth cones. Based on the defective BDNF/TrkB signaling in SMA motoneurons, we tested whether BDNF stimulation can induce an increase in p-profilin levels as shown previously (Dombert et al., 2017). SMA neurons did not show increased p-profilin levels upon BDNF stimulation. Intriguingly, hPLS3 overexpression resulted in enhanced levels of overall profilin and increased p-profilin levels upon BDNF stimulation in SMA motoneurons. Thus, increasing the levels of Pls3 beneficially influences the localization and regulation of actin regulatory proteins such as Arp2/3 or profilin, which are a prerequisite for proper functioning of the actin cytoskeleton, in particular for the translocation and alignment of transmembrane proteins. However, it is possible that other axonal downregulated transcripts, whose corresponding proteins function in actin-bundling and cross-linking such α-actinin (*Actn1*) or filamin A (*Flna*; Stevenson et al., 2012) contribute

to the disturbed actin dynamics thereby influencing translocation of transmembrane proteins.

Interestingly, hPLS3 overexpression in vivo resulted in markedly enhanced BDNF-induced TrkB activation and significantly improved $Ca_v2.1$ "cluster-like" formations in *SMNΔ7* neuromuscular endplates. However, only minor improvements of TrkB localization, G-actin levels and area ratio of the pre- vs. postsynapse were found in NMJs of these animals upon hPLS3 overexpression. This could be due to the postnatal overexpression of hPLS3, as correct F-actin assembly is required already during early embryonic development when motoneurons differentiate and grow out to their targets to form NMJs. Furthermore, as the *SMNΔ7* mouse model is a severely affected disease model, the observed morphological and functional defects due to Smn deficiency are probably only moderately restorable through a partial AAV9-*hPLS3* overexpression (Ackermann et al., 2013; Alrafiah et al., 2018; Kong et al., 2021; McGovern et al., 2015). This has already been reported for SMA patients, since the protective effect of PLS3 is only observed in SMA type 2 and 3 but not in severely affected children with only one or two *SMN2* copies (Oprea et al., 2008) and less severely affected mouse models (Hosseinibarkooie et al., 2016).

In conclusion, our findings reveal that Smn deficiency is associated with the defective activity-induced recruitment of the high-affinity BDNF receptor TrkB to the cell surface at motor axon terminals. As BDNF/TrkB signaling is indispensable for proper motoneuron differentiation and maturation, our data strongly suggest that some of the already described cellular dysregulations are likely to be due to affected BDNF/TrkB signaling. Strikingly, the SMA modifier protein PLS3 is able to rescue TrkB recruitment to the cell surface and to correct localization of VGCCs leading to increased frequency of spontaneous Ca^{2+} transients. Based on our results and encouraged by other studies, we postulate a novel role for PLS3 in supporting correct alignment of transmembrane proteins such as TrkB and $Ca_v2.1/2$ through modulation of F-actin dynamics in axon terminals of motoneurons. This mechanism is a basic prerequisite for proper motoneuron differentiation and maturation probably also in other neurodegenerative disorders beyond SMA.

Materials and methods

Animals

Laboratory mice were housed under controlled conditions in the animal facilities of the Institute of Clinical Neurobiology at the University Hospital Würzburg and Faculty of Medicine, University of Leipzig with access to food and water ad libitum. All described procedures were performed by trained personal following the regulations on animal protection of the German federal law and of the Association for Assessment and Accreditation of Laboratory Animal care, as well as the state authorities. For our studies, various wild-type, SMA mouse models and TrkB-deficient mice were used. CD-1 and FVB mice were obtained from Charles River. *Smn*$^{+/-}$;*SMN2* (RRID:IMSR_JAX:005024) and *Smn*$^{+/-}$;*SMN2*;*SMNΔ7* mice (RRID:IMSR_JAX:005025), initially obtained from Jackson Laboratory were used to breed SMA type I *Smn*$^{-/-}$;*SMN2* mice for the in vitro experiments (Monani et al., 2000) as well as *Smn*$^{-/-}$;*SMN2*;*SMNΔ7* (hereinafter named *SMNΔ7*) for the in vivo experiments in postnatal pups (Le et al., 2005). *Smn*$^{+/+}$;*SMN2*/*Smn*$^{+/-}$;*SMN2* or *Smn*$^{+/+}$;*SMN2*;*SMNΔ7*/*Smn*$^{+/-}$;*SMN2*;*SMNΔ7* were used as controls. For control experiments, TrkB-deficient *Ntrk2*$^{-/-}$ were bred from *Ntrk2*$^{+/-}$ mice originally described elsewhere (Rohrer et al., 1999). Size of the litters varied between 4 and 10. Genotyping of knock-out and transgene alleles was performed using DNA obtained from individual mice tail biopsies. The following primers were used: *Smn*: 5′-CTGGAATTCAATATGCTAGACTGG CCTG-3′ (forward), 5′-CAATCTATCACCTGTTTCAAGGGAGTT GTGG-3′ (reverse 1), 5′-GATGTGCTGCAAGGCGATTAAGTTG-3′ (reverse 2); *SMN2*: 5′-CATACCTTAAAGGAAGCCAC-3′ (forward), 5′-AGGTTCTGAGGTCAGAACAGC-3′ (reverse); *SMNΔ7*: 5′-TCC ATTTCCTCCTGGACCAC-3′ (forward), 5′-ACCCATTCCACTTCC TTT-3′ (reverse); *TrkB*: 5′-ACTGACATCCGTAAGCCAGT-3′ (forward), 5′-ATGTCGCCCTGGCTGAAGTG-3′ (reverse 1), 5′- GGT TCTAAGTACTGTGGTTTCC-3′ (reverse 2).

AAV9-treatment in neonatal mice

The *human PLS3* (*hPLS3*)-containing AAV9 overexpression construct was purchased from VectorBuilder (www.vectorbuilder.com). The open reading frame (ORF) was tagged with an HA-tag and inserted into a self-complementary (sc) AAV9 under a CMV promotor (Vector ID: VB201021-1415qev). As control, an *EGFP*-containing scAAV9 (Vector ID: VB191101-2319suw) was used. AAV9 gene delivery was performed at Carl-Ludwig-Institute for Physiology at Leipzig University as previously described (Simon et al., 2017). In brief, P0/P1 mice were anesthetized by isoflurane inhalation and injected in the right lateral ventricle of the brain with ~5×10^{10} genome copies of AAV9 vectors in a PBS solution containing a vital dye (Fast Green; Sigma-Aldrich).

Muscle preparation and BDNF stimulation

SMNΔ7 mice and aged-matched littermate controls were sacrificed at P5 or P10-11, respectively, and the *Transversus abdominis anterior* (TVA) muscle was dissected from the abdominal wall in pre-warmed physiological solution (135 mM NaCl, 12 mM $NaHCO_3$, 5 mM KCl, 1 mM $MgCl_2$, 20 mM Glucose, 2 mM $CaCl_2$). For BDNF stimulation experiments, the muscle for BDNF treatment was placed in physiological solution containing 500 ng/ml BDNF and incubated for 30 min shaking on a heating plate, while the untreated muscle was kept in physiological solution without BDNF for 30 min. Subsequently, the medium was exchanged to physiological solution without $CaCl_2$ for 5–10 min prior to fixation of the muscle with cold methanol-free 4% formaldehyde (Pierce, Thermo Fisher Scientific) for 90 min. Following three washing steps with PBS, they were kept in PBS until processing with the immunohistochemistry.

TVA immunohistochemistry

All steps were performed on an orbital shaker at room temperature (RT), if not stated otherwise. In brief, muscles were incubated with 0.1 M glycine (in PBS) for 30 min, permeabilized with 1% Triton X-100 in (TBS-T) for 2 × 5 min, 2 × 10 min, and 2 × 30 min and incubated in 10% bovine serum albumin (BSA in TBS-T) for 3 h prior to antibody staining. Vitamin D-binding

protein (DBP; Lee et al., 2013) was used for the visualization of G-actin. For this experiment, TVA muscles were first exposed to ice-cold acetone for 7 min and then incubated with 15 µg/ml DBP (345802; Merck, in TBS-T) for 2 h at RT. After postfixation with methanol-free 4% formaldehyde for 30 min, the muscles were washed thrice with TBS-T, permeabilized with 1% Triton X-100 in (TBS-T) for 2 × 30 min and incubated in 10% BSA (in TBS-T) for 3 h. Primary antibodies were incubated in 2.5% BSA and 0.5–1 % Triton X-100 (in TBS-T) for 3 d shaking at 4°C. Afterwards, samples were washed thrice with TBS-T and secondary antibodies were incubated in 2.5% BSA and 0.05% Triton X-100 (in TBS-T) for 1 h. After final washing steps with TBS-T for 90 min, muscles were mounted on glass microscope slides using Aqua-Poly/Mount (18606; Polysciences). The following primary and secondary antibodies were used: polyclonal rabbit Ca^{2+} channel P/Q-type alpha-1A antibody ($Ca_v2.1$; 1:250, 152 203, RRID:AB_2619841; Synaptic systems), polyclonal rabbit anti-DBP (1:150, PA5-19802, RRID:AB_10989680; Thermo Fisher Scientific), polyclonal chicken anti-Neurofilament H (1:1,000, AB5539, RRID:AB_11212161; Sigma-Aldrich), monoclonal rabbit anti-p-TrkB (1:250, 4621, RRID:AB_916186; Cell signaling), polyclonal guinea pig anti-Synaptophysin-1 (1:500, 101 004, RRID: AB_1210382; Synaptic systems), polyclonal goat anti-TrkB (1: 300, AF1494, RRID:AB_2155264; R&D systems), Alexa Fluor 488 AffiniPure donkey anti-guinea pig IgG (H + L; 1:500, 706-545-148, RRID:AB_2340472; Jackson Immuno Research), Cy3 AffiniPure donkey anti-chicken IgY (IgG; H + L; 1:500, 703-165-155, RRID:AB_2340363; Jackson Immuno Research), Cy3 AffiniPure donkey anti-goat IgG (H + L; 1:500, 705-165-003, RRID: AB_2340411; Jackson Immuno Research), Cy3 AffiniPure donkey anti-guinea pig IgG (H + L; 1:500, 706-165-148, RRID: AB_2340460; Jackson Immuno Research), Cy3 AffiniPure donkey anti-rabbit IgG (H + L; 1:500, 711-165-152, RRID:AB_2307443; Jackson Immuno Research), Cy5 AffiniPure donkey anti-goat IgG (H + L; 1:500, Jackson Immuno Research, 705-175-003), Cy5 AffiniPure donkey anti-guinea pig IgG (H + L; 1.500, 706-175-148, RRID:AB_2340462; Jackson Immuno Research), Alexa Fluor 647 donkey anti-rabbit IgG (H + L) highly cross-adsorbed (1:600, A-31573, RRID:AB_2536183; Thermo Fisher Scientific). Postsynaptic nicotinic acetylcholine receptors were labeled with Alexa Fluor 488 α-Bungarotoxin (1:500, B13422; Invitrogen).

Spinal cord immunohistochemistry

Spinal cord immunostainings were performed as previously described (Buettner et al., 2021). In detail, P10-P11 mice were perfused with PBS and 4% PFA followed by a 4% PFA postfixation over night at 4°C. On the next day, the spinal cord was briefly washed with PBS. Subsequently, the spinal lumbar L1 segment was dissected and embedded in warm 5% agar and serial transverse sections (75 µm) were cut at the vibratome. The sections were blocked with 5% normal donkey serum in 0.01 M PBS with 0.3% Triton X-100 (in PBS-T; pH 7.4) for 90 min and incubated with the primary antibodies over night at RT. On the next day, after six times of 10 min PBS washes, sections were incubated with the secondary antibodies diluted in PBS-T for 3 h. Following six washing steps with PBS for 10 min, sections were mounted on slides and cover-slipped with an anti-fading solution made of Glycerol:PBS (3:7). The following primary and secondary antibodies were used: Polyclonal goat anti-ChAT (1: 500, AB144P, RRID:AB_2079751; Merck), polyclonal chicken anti-GFP (1:2,000, ab13970, RRID:AB_300798; Abcam), monoclonal rat anti-HA (1:500, 11867423001, RRID:AB_390918; Roche), Alexa Fluor 488 AffiniPure donkey anti-chicken IgY (IgG; H + L; 1:1,000, 703-545-155, RRID:AB_2340375; Jackson Immuno Research), Cy3 AffiniPure donkey anti-rat IgG (H + L; 1: 1,000, 712-165-150, RRID:AB_2340666; Jackson Immuno Research), Alexa Fluor 647 AffiniPure donkey anti-goat IgG (1:1,000, 705-605-003, RRID:AB_2340436; Jackson Immuno Research).

Cloning of lentiviral constructs and packaging

To specifically knockdown endogenous Smn and Pls3 in motoneurons, shRNA oligonucleotides targeting the murine *Smn* and *Pls3* were designed and introduced into a GFP-expressing pSIH-H1 shRNA vector (System Bioscience) according to the manufacturer's protocol. As control, an empty pSIH-H1 shRNA vector (GFP) or Luciferase-containing pSIH-H1 shRNA vector (sh*Luci*) was used. The following antisense sequences were used for cloning: *Smn*: 5′-GAAGAATGCCACAACTCCC-3′; *Pls3*: 5′-CTC ATGGTGGATGGTGACAG-3′. For generation of the *TrkB-GFP* construct, the coding sequence of *GFP* was fused to the C-terminus of the murine *TrkB* coding sequence and inserted into a FuVal vector backbone under the ubiquitin promotor harboring a Kozak sequence. Correct plasmid insertion was checked by sequencing (LGC Genomics GmbH) and plasmid purification for lentivirus production was performed with the NucleoBond Xtra Midi plasmid purification kit (Machery Nagel). For overexpression of *hPLS3*, the constructs were obtained from VectorBuilder (www.vectorbuilder.com). The ORF was inserted under the ubiquitin promoter into a mammalian gene expression vector containing mCherry (Vector ID: VB200130-1089naj). As control, a mCherry containing vector (Vector ID: VB181226-1081ctz) was used. Lentivirus packaging was performed in HEK293TN cells transfected through TransIT-293 (Mirus) with the corresponding plasmid together with pCMV-VSVG and pCMVΔR8.91 helper plasmids (Rehberg et al., 2008). Upon ultracentrifugation at 25,000 rpm (SW 32 Ti rotor, Beckman) for 120 min at 4°C, the viral supernatant was harvested and stored at −80°C.

Primary embryonic motoneuron cell culture and lentiviral transduction

The primary motoneuron cell culture was performed according to Wiese et al. (2010). In detail, the lumbar part of the spinal cord was dissected from mouse embryos on embryonic day (E) 12.5 and digested with 0.1% trypsin (Worthington). After gentle trituration, the cells were enriched through anti-$p75^{NTR}$ antibody panning (MLR2, M-009-100, RRID:AB_2492396; Biosensis) and plated onto poly-DL-ornithine hydrobromide (PORN; 0.5 mg/ml, P8638; Sigma-Aldrich) and laminin-221/211 (2.5 µg/ml, CC085; Merck) coated glass coverslips. For RNA and Western blot analysis, the cells were plated on PORN/laminin-111 (2.5 µg/ml, 23017-015; Thermo Fisher Scientific) coated 24-well plates. For live-cell imaging experiments, motoneurons were

plated on PORN/laminin-221/211 coated 35 mm high µ-dishes (81156; Ibidi). Compartmentalized motoneuron cultures were maintained in microfluidic chambers (Xona Microfluidics, SND 150) pre-coated with PORN/laminin-111. For lentiviral transduction, the motoneuron suspension was incubated with the lentiviral particles for 15 min prior to plating. Motoneurons were maintained in complete medium (Neurobasal medium [NB]; Life Technologies) supplied with 500 µM Glutamax (Life Technologies), 2% B27 (Life Technologies), 2% heat-inactivated horse serum (Linaris), as well as neurotrophic factors CNTF (5 ng/ml) and BDNF (2 ng/ml). For compartmentalized chambers, a BDNF concentration gradient was established to achieve a directed axonal growth from no BDNF at the somatodendritic side to 20 ng/ml BDNF at the axonal side, while 5 ng/ml CNTF was added on both sides. The cells were kept at 37°C and 5% CO_2, and the medium was exchanged on the first day in vitro (DIV) and then every second or third day. Standard experiments were performed on DIV5. RT-PCR, Western blot analysis or experiments with lentiviral transduced cells were performed on DIV7.

BDNF stimulation

For BDNF stimulation experiments, cells were grown in complete medium supplemented with BDNF (2 ng/ml) and CNTF (5 ng/ml). Depending on the experimental setup, on DIV4 or DIV6, motoneurons were deprived from BDNF for 16–24 h prior to the experiments. Cells were washed thrice with NB medium, and complete medium supplemented with CNTF (5 ng/ml) was added. On DIV5/DIV7, motoneurons were incubated with 100 ng/ml BDNF in complete medium for 15 min. Subsequently, cells were washed with NB medium and fixed with methanol-free 4% formaldehyde for 10 min.

Live-cell immunocytochemistry for TrkB surface labeling

Live-cell immunocytochemistry was performed to exclusively label TrkB presented at the plasma membrane. Motoneurons were cultured on laminin-221/211 coated glass coverslips and deprived from BDNF 1 d prior to the experiments as described before. On DIV5/DIV7, motoneurons were placed on parafilm and immediately covered with pre-warmed complete medium. According to the experimental design, cells were pre-treated with Cytochalasin D (C2618; 0.5 µM, 30 min; Sigma-Aldrich), Nocodazole (M1404; 10 µM; Sigma-Aldrich, 2 h), Cycloheximide (01810; 20 µM; Sigma-Aldrich, 1 h) or CK-666 (SML0006; 50 µM; Sigma-Aldrich, 30 min + 15 min during stimulation/recovery). For BDNF stimulation, the medium was exchanged with 100 ng/ml BDNF-containing medium for 5 min or 15 min at 37°C. For cAMP stimulation, the medium was exchanged with 100 µM 8-(4- Chlorophenylthio) adenosine-3′, 5′- cyclic monophosphate (8-CPT-cAMP) containing complete medium for 20 min at 37°C. Afterward, cells were washed with cold complete medium and placed on ice. The antibody against the extracellular domain of TrkB (1:200, polyclonal rabbit anti-TrkB, 07-225, RRID: AB_310445; Merck) was diluted in cold complete medium and added for 45 min. After washing with PBS, the secondary antibody (Alexa Fluor 488 AffiniPure donkey anti-rabbit IgG [H + L], 1:300, Jackson Immuno Research, 711-545-152, RRID:AB_2313584 or Alexa Fluor 647 donkey anti-rabbit IgG [H + L] highly cross-adsorbed, 1:400, A-31573, RRID:AB_2536183; Thermo Fisher Scientific) diluted in cold complete medium was incubated for 30 min. Following three washing steps with cold PBS cells were fixed with methanol-free 4% formaldehyde for 5 min and standard immunofluorescence protocol without permeabilizing agents like Triton X-100 was used to visualize intracellular proteins.

TrkB recycling assay (double live-cell immunocytochemistry for TrkB surface labeling)

For double live-cell-labeling experiments, DIV5/DIV7 motoneurons, that were previously deprived from BDNF, were placed on parafilm and immediately covered with pre-warmed complete medium. The cells were washed with cold complete medium and placed on ice. TrkB antibody (1:200, polyclonal rabbit anti-TrkB, 07-225, RRID:AB_310445; Merck) diluted in cold complete medium was added for 30 min, followed by three washing steps with cold PBS and Alexa Fluor 488 AffiniPure donkey anti-rabbit IgG (H + L) incubation (1:300, 711-545-152, RRID:AB_2313584; Jackson Immuno Research) diluted in cold complete medium for 25 min. After a washing step with complete medium, motoneurons were removed from ice and 100 ng/ml BDNF-containing pre-warmed complete medium was added for 5 min at 37°C. After that, remaining antibodies were washed off twice with 1 mM EDTA in complete medium and cells were incubated with warm complete medium for 10 min for recovery. Subsequently, motoneurons were placed back on ice and incubated with the TrkB antibody (1:200, polyclonal rabbit anti-TrkB, 07-225, RRID:AB_310445; Merck) diluted in cold complete medium for 30 min. Again, following three washing steps with cold PBS, the cells were incubated with Alexa Fluor 647 donkey anti-rabbit IgG (H + L) highly cross-adsorbed (1: 400, A-31573, RRID:AB_2536183; Thermo Fisher Scientific) diluted in cold complete medium for 25 min. Following three washing steps with cold PBS, cells were fixed with methanol-free 4% formaldehyde for 5 min and standard immunofluorescence protocol omitting permeabilization was used to visualize intracellular proteins.

Immunocytochemistry of cultured motoneurons

Motoneurons were grown on laminin-221/211 coated glass coverslips until DIV5/DIV7, fixed for 5–10 min with methanol-free 4% formaldehyde and then washed thrice with PBS. Coverslips were placed on parafilm and covered with TBS-T before they were permeabilized with 0.3% Triton X-100 (except for TrkB stainings) for 20 min. For G-actin staining using DBP, motoneurons were exposed to ice-cold acetone for 5 min followed by incubation with 5 µg/ml DBP for 1 h at RT. Following three washing steps with TBS-T, they were incubated with 10% BSA in TBS-T for 1 h at RT. Primary antibodies were incubated in 1% BSA in TBS-T overnight at 4°C. The next day, cells were washed with TBS-T thrice, followed by incubation with the secondary antibodies in 1% BSA in TBS-T for 1 h at RT. Lastly, cells were washed thrice with TBS-T and mounted on glass microscope slides using Aqua-Poly/Mount (18606; Polysciences) for confocal imaging and ProLong Glass (P36980; Thermo Fisher Scientific/ Invitrogen) for high-resolution imaging. The following primary

and secondary antibodies were used: monoclonal mouse anti-Arp3 (1:200, A5979, RRID:AB_476749; Sigma-Aldrich), polyclonal guinea pig anti-Ca^{2+} channel N-type alpha-1B (Ca_vN; 1:500, 152 305, RRID:AB_2619845; Synaptic systems), polyclonal rabbit anti-DBP (1:500, PA5-19802, RRID:AB_10989680; Thermo Fisher Scientific), monoclonal rat anti-mCherry (1:1,000, M11217, RRID: AB_2536611; Thermo Fisher Scientific/Invitrogen), monoclonal mouse anti-myosin VI (1:250, GTX11095, RRID:AB_369989; GeneTex), monoclonal rabbit anti-p-Akt (1:500, 4060, RRID: AB_2315049; Cell signaling), polyclonal rabbit anti-Plastin 3 middle region (1:100, ARP56623_P050, RRID:AB_10642988; Aviva systems biology), monoclonal rabbit anti-p-TrkB (1:500, 4621, RRID:AB_916186; Cell signaling), polyclonal guinea pig anti-Synaptophysin-1 (1:1,000, 101 004, RRID:AB_1210382; Synaptic systems), polyclonal rabbit anti-TrkB (1:1,000, 07-225, RRID:AB_310445; Merck), Alexa Fluor 488 AffiniPure donkey anti-rabbit IgG (H + L; 1:600, 711-545-152, RRID:AB_2313584; Jackson Immuno Research), Alexa Fluor 488 AffiniPure donkey anti-guinea pig IgG (H + L; 1:500, 706-545-148, RRID: AB_2340472; Jackson Immuno Research), Cy3 AffiniPure donkey anti-guinea pig IgG (H + L; 1:500, 706-165-148, RRID: AB_2340460; Jackson Immuno Research), Cy3 AffiniPure donkey anti-mouse IgG (H + L; 1:500, 715-165-151, RRID:AB_2315777; Jackson Immuno Research), Cy3 AffiniPure donkey anti-rabbit IgG (H + L; 1:500, 711-165-152, RRID:AB_2307443; Jackson Immuno Research), Cy3 AffiniPure donkey anti-rat IgG (H + L; 1: 500, Jackson Immuno Research, 712-165-150, RRID:AB_2340666), Cy5 AffiniPure donkey anti-guinea pig IgG (H + L; 1:500, 706-175-148, RRID:AB_2340462; Jackson Immuno Research), Cy5 AffiniPure goat anti-mouse IgG (H + L; 1:500, 115-175-146, RRID: AB_2338713; Jackson Immuno Research), Alexa Fluor 647 donkey anti-rabbit IgG (H + L) highly cross-adsorbed (1:800, A-31573, RRID:AB_2536183; Thermo Fisher Scientific). F-actin was visualized either with ActinGreen 488 ReadyProbes Reagent (1:50, R37110; Invitrogen), ActinRed 555 ReadyProbes Reagent (Rhodamine Phalloidin, 1:50, R37112; Invitrogen) or with Alexa Fluor 546 Phalloidin (1:50, A22283; Invitrogen).

Image acquisition and quantification

Image acquisition of mounted samples was performed at RT with an Olympus Fluoview 1,000 confocal system equipped with a UPLSAPO 60×/1.35 NA oil objective, a FVD10 SPD spectral detector and the FV10-ASW 4.2 software. For motoneurons, single stack images were taken with 16-bit, 512 × 512-pixel resolution, and for NMJs 16-bit 0.5 µm z-stack images with 1,024 × 1,024-pixel resolution were acquired. Identical settings were applied within one set of experiments. Quantification was done with unprocessed images using Fiji and the "sum slices" projection was used for z-stacks. The mean gray value per area of the immunosignal was quantified in the region of interest (ROI) and the background signal was subtracted. For normalization, all values originating from one experiment were divided by the mean of the corresponding untreated control group to correct for inter-experimental variations. For TrkB recycling assay, the total number of TrkB-A488 and TrkB-A647 immunosignals was counted after linear brightness and contrast adjustments. TrkB-A647, as recovered receptors after BDNF stimulation were counted as the percentage of TrkB-A488, as endocytosed receptors that have been at the cell surface prior to BDNF stimulation. The amount of co-localizing recycled TrkB was determined with JaCoP plugin based on "Objects based methods" and "Geometrical centre" analysis and used to calculate the percentage of recycled TrkB (recovered receptors that previously have been on the cell surface). Illustration and statistical analysis were performed with GraphPad Prism 6. To obtain higher resolution pictures, structured illumination microscopy (SIM) was performed on a Zeiss ELYRA S.1 or Zeiss ELYRA 7 system, each equipped with a plan APO 63×/1.4 NA oil objective and sCMOS pco.edge cameras. Images were processed with the Zeiss software ZEN (ZEN 2012 SP5 FP3 for the ELYRA S.1 and ZEN 3.0 SR FP2 for the ELYRA 7 system, respectively) using automated standard settings. SIM images were corrected for chromatic aberration by channel alignment created with Tetraspecks (T14792; Thermo Fisher Scientific). "Maximum intensity" projected SI-images were generated with Fiji and Brightness/Contrast were adjusted for better visibility.

Live-cell imaging of actin dynamics and data quantification

For analysis of actin dynamics, motoneurons were grown on PORN/laminin-221/211 coated 35 mm high µ-dishes (81156; Ibidi). On DIV7, cells were incubated with 100 nM SiR-actin (far-red and cell-permeable probe for F-actin visualization, tebu-bio, SC006) for 2 h. After washing with PBS, pre-warmed Tyrode's solution (125 mM NaCl, 2 mM KCl, 2 mM $CaCl_2$, 2 mM $MgCl_2$, 30 mM glucose, 25 mM HEPES, pH 7.4) was added and chamber was placed into Tokai Hit stage incubator for imaging at 37°C with constant 5% CO_2 supply. Imaging was performed using the Nikon's Eclipse TE2000 inverted epifluorescence microscope equipped with a plan APO VC 60×/1.4 NA objective, a perfect focus system and NIS-Elements AR 4.40.00 software. A fluorescent LED light with an excitation wavelength of 635 nm was used. 16-bit, 1,024 × 1,022-pixel images (2 × 2 binning) were acquired every 15 s over a time period of 20 min (exposure time 200 ms) with the ORCA Flash 4.0 V2 C11440-22C camera (Hamamatsu Photonics). For quantification of actin dynamics within single filopodia of growth cones Fiji was used to generate maximum intensity projections and identify the total length of each filopodia starting at the growth cone center. The ROI was transferred to the time-lapse video and a kymograph was generated using the corresponding multi kymograph plugin. The moved distance of single filopodia (y axis, length in µm) as well as the velocity (µm/min) of single filopodia movements (y axis, length in µm divided by x axis, time in minutes) derived from various growth cones were illustrated.

Calcium imaging and data analysis

Calcium imaging was performed on DIV7 motoneurons plated on PORN/laminin-221/211 coated 35 mm high µ-dishes (81156; Ibidi). Cells were incubated with 5 µM Oregon Green 488 BAPTA-1, AM (O6807; Invitrogen, in Pluronic F-127; Thermo Fisher Scientific) or Cal-590 AM (ABD-20511; Biomol, in Pluronic F-127; Thermo Fisher Scientific) diluted in calcium imaging buffer (135 mM NaCl, 1 mM $MgCl_2$, 10 mM HEPES, 1 mM $CaCl_2$, 6 mM KCl, 5.5 mM Glucose, pH 7.4) for 15 min at 37°C. Upon

three washing steps, cells were covered with calcium imaging buffer and placed into Tokai Hit stage incubator for imaging at 37°C with constant 5% CO_2 supply. Calcium imaging was performed at the Nikon's Eclipse TE2000 inverted epifluorescence microscope equipped with a plan APO VC 60×/1.4 NA objective, a perfect focus system and NIS-Elements AR 4.40.00 software. A fluorescence LED light source was used for excitation at 470 nm (for Oregon Green) or 590 nm (for Cal-590 AM). 16-bit, 1,024 × 1,022-pixel pictures (2 × 2 binning) were taken at a frequency of 2 Hz over 5 min (exposure time 100 ms) at the ORCA Flash 4.0 V2 C11440-22C camera (Hamamatsu Photonics). The resulting 601 frame videos were analyzed with Fiji. Growth cones were defined as region of interest and a dynamic Z-axis profile, normalized against the average of the first 20 frames (F/F0), was plotted. Calcium spikes were counted using the BAR Plugin.

Live-cell imaging of TrkB-GFP

TrkB-GFP live-cell imaging was performed on motoneurons co-transduced with LV-*TrkB-GFP* and LV-*mCh* or LV-*hPLS3* respectively, plated on PORN/laminin-221/211 coated 35 mm high µ-dishes (81156; Ibidi). ON DIV7, motoneurons were washed with pre-warmed Tyrode's solution (125 mM NaCl, 2 mM KCl, 2 mM $CaCl_2$, 2 mM $MgCl_2$, 30 mM glucose, 25 mM HEPES, pH 7.4) and incubated with 100 µM 8-(4- Chlorophenylthio) adenosine-3', 5'- cyclic monophosphate (8-CPT-cAMP) containing Tyrode's solution for recording. Imaging was performed at the Nikon's Eclipse TE2000 inverted epifluorescence microscope equipped with a plan APO VC 60×/1.4 NA objective, a perfect focus system and NIS-Elements AR 4.40.00 software. A fluorescence LED light source was used for excitation at 470 nm. 16-bit, 1,024 × 1,022-pixel pictures (2 × 2 binning) were acquired every ∼ 2.5 s over a time period of 10 min (exposure time 100 ms) using the ORCA Flash 4.0 V2 C11440-22C camera (Hamamatsu Photonics). The resulting videos were analyzed with Fiji.

RNA-seq and analysis

For RNA-seq, motoneurons were transduced with *Smn* knockdown or GFP control lentiviruses and cultured in microfluidic chambers (Xona Microfluidics, SND 150; Saal et al., 2014). On DIV7, RNA was extracted from the somatodendritic and the axonal compartments and whole-transcriptome profiling was used for cDNA amplification and library generation (Briese et al., 2016). The corresponding GFP control samples were described previously (Briese et al., 2018) and processed in parallel to the Smn knockdown samples described here. Libraries were sequenced on an Illumina MiSeq System and reads were mapped to the mouse genome with Star version 2.4.0d (https://code.google.com/p/rna-star/). Calculation of fragments per kilobase of transcript per million mapped reads (FPKM) values and analysis of differential gene expression was done using the Cufflinks package version 2.2.1 (http://cufflinks.cbcb.umd.edu/; Briese et al., 2016). For GO term analysis the Database for Annotation, Visualization and Integrated Discovery (DAVID) was used (Huang et al., 2009). As background datasets, the 10,433 and 11,127 transcripts previously detected in the somatodendritic and axonal compartment, respectively of wild-type motoneurons were used (Briese et al., 2016). The sequencing data from Smn knockdown motoneurons described in this publication are accessible in NCBI's Gene Expression Omnibus through GEO Series accession no. GSE197638 (Edgar et al., 2002).

Western blot analysis

For Western blot analysis to quantify the total protein amount in the cells, motoneurons were cultured on PORN/laminin-111 coated 24-wells until DIV7. Cells were deprived from BDNF on DIV6 as previously described. On DIV7, cells were stimulated with 100 ng/ml BDNF for 15 min, washed with HBSS and directly lysed in Laemmli buffer (125 mM Tris, pH 6.8, 10% SDS, 50% glycerol, 25% β-mercaptoethanol and 0.2% bromophenol blue). Lysates were boiled for 5 min at 99°C, separated on a 4–12% gradient SDS-PAGE gel and transferred to a polyvinylidene fluoride membrane (BioRad). Unspecific binding sites were blocked with 5% milk (TBS-T) for 1 h and probed with the following primary antibodies in TBS-T over night at 4°C. Monoclonal rabbit anti-p-TrkB (1:1,000, 4621, RRID:AB_916186; Cell signaling), polyclonal rabbit anti-TrkB (1:1,000, 07-225, RRID:AB_310445; Merck), monoclonal mouse anti-beta actin (1:3,000, GTX26276, RRID:AB_367161; GeneTex). Following three washing steps, the membrane was incubated with horseradish-peroxidase (HRP)-conjugated secondary antibodies for 1 h at RT and immunodetection was performed using Amersham ECL Western blotting Detection Reagent (Cytiva) and x-ray films (Fuji super RX). The following secondary antibodies were used: peroxidase AffiniPure goat anti-rabbit IgG (H + L; 1:10,000, 111-035-144, RRID:AB_2307391; Jackson Immuno Research) and peroxidase AffiniPure goat anti-mouse IgG (H + L; 1:10,000, 115-035-003, RRID:AB_10015289; Jackson Immuno Research).

Real-time-PCR (RT-PCR)

RNA from DIV7 motoneurons cultured on PORN/laminin-111-coated 24-wells was isolated using the NucleoSpin RNA kit (Macherey-Nagel) and transcribed in cDNA with the help of the RevertAid First Strand cDNA Synthesis Kit (Thermo Fisher Scientific). RT-PCR was performed using 1:5 diluted cDNA and Luminaris HiGreen qPCR Master Mix (Thermo Fisher Scientific) on a LightCycler 1.5 thermal cycler (Roche). Absolute copy numbers of *TrkB* and *Plastin 3* were normalized to the absolute copy numbers of *Gapdh* as reference gene. The following primers were used: murine *TrkB*: 5′-CGGGAGCATCTCTCGGTCTAT-3′ (forward), 5′-CTGGCAGAGTCATCGTCGTTG-3′ (reverse); murine *Gapdh*: 5′-GCAAATTCAACGGCACA-3′ (forward), 5′-GTC GTGGAGTCTACTGGTG-3′ (reverse); murine *Pls3*: 5′-CAAGCC TCCATACCCAAAGC-3′ (forward), 5′-CCATCGTTCAGGTCTTGT CC-3′ (reverse); human *PLS3*: 5′-GAACGTTGAGTGAAGCTGGA-3′ (forward), 5′-TTGCCACTCTTCACAAGGTC-3′ (reverse).

Statistics

For statistical analysis, GraphPad Prism 6 was used. For all data sets, at least three independent experiments were performed, and "N" represents the set of experiments while "*n*" indicates the number of independent data points. For $n < 40$, the data is shown as mean ± SD; for $n > 40$ the results are shown as mean ± SEM. Normal distribution was tested using D'Agostino & Pearson omnibus normality test. Two-tailed unpaired *t* tests were used

for normally distributed data sets and group analyses (*Smn/Pls3* FPKMs). For not equal distributed data sets, Mann–Whitney U-test was used for comparison of two groups while more groups were analyzed by one-way analysis of variance (ANOVA) Kruskal–Wallis test and Dunn's Multiple Comparison post-hoc test. Significance is indicated as n.s. (not significant) if $P > 0.05$, * if $P < 0.05$, ** if $P < 0.01$, *** if $P < 0.001$, and **** if $P < 0.0001$. Data is shown as scatter dot plots with bars/bar plots for FPKMs.

The final processing of representative images and graphs was performed with Adobe Illustrator v 25.2.2 software.

Online supplemental material

Fig. S1 shows disturbed TrkB localization and phosphorylation upon BDNF stimulation in *SMNΔ7* NMJs at P5 and Western blot analysis of TrkB and p-TrkB in control and SMA motoneuron whole-cell lysates. Fig. S2 demonstrates the antibody specificity of TrkB and p-TrkB antibodies used in this study. Fig. S3 shows that reduced profilin levels and p-profilin levels after BDNF stimulation in SMA motoneurons can be rescued by hPLS3 overexpression. Fig. S4 shows robust AAV9-delivered hPLS3 or GFP expression in the L1 spinal segment of injected P10 control mice. Table S1 contains the transcriptome analysis of the somatodendritic and axonal compartment of Smn knockdown and GFP-expressing control motoneurons. Table S2 contains the GO term analysis of significantly down- and upregulated transcripts in the somatodendritic and axonal compartment of Smn knockdown motoneurons. Videos 1, 2, and 3 show TrkB-GFP movements upon cAMP stimulation in Video 1 LV-*mCh* transduced control motoneurons, Video 2 LV-*mCh* transduced Smn-deficient motoneurons, and Video 3 LV-*hPLS3* transduced Smn-deficient motoneurons.

Acknowledgments

We thank Nicole Rachor and Hildegard Troll for skilful technical support, Manas Kshirsagar for providing the TrkB-GFP lentiviral particles. The animal facility for the stock breeding of the mouse lines and Marcus Behringer for assistance with SIM.

Work in the authors' lab is supported by the Deutsche Forschungsgemeinschaft, Grants JA 1823/3-1 to S. Jablonka, SE 697/6-1 to M. Sendtner, SI 1969/2-1 and SI 1969/3-1 to C.M. Simon, BR 4910/2–1 to M. Briese; by a grant from Picoquant to M. Sendtner; by Cure SMA (JAB1920) to S. Jablonka and SMA Europe to C. Simon.

Author contributions: S. Jablonka and M. Sendtner conceived the project and thereafter S. Jablonka, M. Sendtner and L. Hennlein designed the experiments. L. Hennlein performed most of the experiments including TVA preparations, clonings, motoneuron cultures, TVA and motoneuron immunostainings, image acquisition and live-cell imaging, Western blot analysis and RT-PCR analysis as well as analysis of the data. H. Ghanawi performed the cloning of sh*Pls3*, helped with motoneuron cultures, Western blot analysis and RT-PCRs. C.M. Simon and F. Gerstner performed the AAV9-treatment in neonatal mice, TVA preparations and spinal cord immunohistochemistry. E. Palominos-Garcia performed the motoneuron $Ca_v2.2$ immunostainings and calcium imaging and data analysis under the assistance of L. Hennlein. L. Saal-Bauernschubert performed the cloning of sh*Smn* and the compartmentalized motoneuron cultures and their preparation for RNA-seq. S. Appenzeller and M. Briese performed bioinformatic analysis of the RNA-seq data. E. Yildirim helped with calcium imaging. M. Moradi and C. Deng provided the TrkB-GFP construct. M. Moradi helped with cloning and live-cell imaging. M. Sauer and T. Klein performed SIM on the ELYRA 7. L. Hennlein prepared the graphical abstract, figures, and additional files. L. Hennlein and S. Jablonka wrote the manuscript with the assistance of all co-authors.

Disclosures: The authors declare no competing interests exist.

Submitted: 28 April 2022
Revised: 12 October 2022
Accepted: 8 December 2022

References

Ackermann, B., S. Kröber, L. Torres-Benito, A. Borgmann, M. Peters, S.M. Hosseini Barkooie, R. Tejero, M. Jakubik, J. Schreml, J. Milbradt, et al. 2013. Plastin 3 ameliorates spinal muscular atrophy via delayed axon pruning and improves neuromuscular junction functionality. *Hum. Mol. Genet.* 22:1328–1347. https://doi.org/10.1093/hmg/dds540

Alrafiah, A., E. Karyka, I. Coldicott, K. Iremonger, K.E. Lewis, K. Ning, and M. Azzouz. 2018. Plastin 3 promotes motor neuron axonal growth and extends survival in a mouse model of spinal muscular atrophy. *Mol. Ther. Methods Clin. Dev.* 9:81–89. https://doi.org/10.1016/j.omtm.2018.01.007

Amidfar, M., J. de Oliveira, E. Kucharska, J. Budni, and Y.K. Kim. 2020. The role of CREB and BDNF in neurobiology and treatment of Alzheimer's disease. *Life Sci.* 257:118020. https://doi.org/10.1016/j.lfs.2020.118020

Andreska, T., P. Lüningschrör, and M. Sendtner. 2020. Regulation of TrkB cell surface expression-a mechanism for modulation of neuronal responsiveness to brain-derived neurotrophic factor. *Cell Tissue Res.* 382:5–14. https://doi.org/10.1007/s00441-020-03224-7

Antoine, M., K.L. Patrick, J. Soret, P. Duc, F. Rage, R. Cacciottolo, K.E. Nissen, R.J. Cauchi, N.J. Krogan, C. Guthrie, et al. 2020. Splicing defects of the profilin gene alter actin dynamics in an *S. pombe* SMN mutant. *iScience.* 23:100809. https://doi.org/10.1016/j.isci.2019.100809

Arakawa, Y., M. Sendtner, and H. Thoenen. 1990. Survival effect of ciliary neurotrophic factor (CNTF) on chick embryonic motoneurons in culture: Comparison with other neurotrophic factors and cytokines. *J. Neurosci.* 10:3507–3515. https://doi.org/10.1523/JNEUROSCI.10-11-03507.1990

Bowerman, M., C.L. Anderson, A. Beauvais, P.P. Boyl, W. Witke, and R. Kothary. 2009. SMN, profilin IIa and plastin 3: A link between the deregulation of actin dynamics and SMA pathogenesis. *Mol. Cell. Neurosci.* 42:66–74. https://doi.org/10.1016/j.mcn.2009.05.009

Bowerman, M., D. Shafey, and R. Kothary. 2007. Smn depletion alters profilin II expression and leads to upregulation of the RhoA/ROCK pathway and defects in neuronal integrity. *J. Mol. Neurosci.* 32:120–131. https://doi.org/10.1007/s12031-007-0024-5

Briese, M., L. Saal-Bauernschubert, C. Ji, M. Moradi, H. Ghanawi, M. Uhl, S. Appenzeller, R. Backofen, and M. Sendtner. 2018. hnRNP R and its main interactor, the noncoding RNA 7SK, coregulate the axonal transcriptome of motoneurons. *Proc. Natl. Acad. Sci. USA.* 115:E2859–E2868. https://doi.org/10.1073/pnas.1721670115

Briese, M., L. Saal, S. Appenzeller, M. Moradi, A. Baluapuri, and M. Sendtner. 2016. Whole transcriptome profiling reveals the RNA content of motor axons. *Nucleic Acids Res.* 44:e33. https://doi.org/10.1093/nar/gkv1027

Buettner, J.M., J.K. Sime Longang, F. Gerstner, K.S. Apel, B. Blanco-Redondo, L. Sowoidnich, E. Janzen, T. Langenhan, B. Wirth, and C.M. Simon. 2021. Central synaptopathy is the most conserved feature of motor circuit pathology across spinal muscular atrophy mouse models. *iScience.* 24:103376. https://doi.org/10.1016/j.isci.2021.103376

Chao, M.V., and B.L. Hempstead. 1995. p75 and Trk: A two-receptor system. *Trends Neurosci.* 18:321–326. https://doi.org/10.1016/0166-2236(95)93922-K

Cheng, P.L., A.H. Song, Y.H. Wong, S. Wang, X. Zhang, and M.M. Poo. 2011. Self-amplifying autocrine actions of BDNF in axon development. *Proc. Natl. Acad. Sci. USA*. 108:18430–18435. https://doi.org/10.1073/pnas.1115907108

Deng, C., M. Moradi, S. Reinhard, C. Ji, S. Jablonka, L. Hennlein, P. Lüningschrör, S. Doose, M. Sauer, and M. Sendtner. 2021. Dynamic remodeling of ribosomes and endoplasmic reticulum in axon terminals of motoneurons. *J. Cell Sci.* 134:134. https://doi.org/10.1242/jcs.258785

Dimitriadi, M., J.N. Sleigh, A. Walker, H.C. Chang, A. Sen, G. Kalloo, J. Harris, T. Barsby, M.B. Walsh, J.S. Satterlee, et al. 2010. Conserved genes act as modifiers of invertebrate SMN loss of function defects. *PLoS Genet.* 6: e1001172. https://doi.org/10.1371/journal.pgen.1001172

Dombert, B., S. Balk, P. Lüningschrör, M. Moradi, R. Sivadasan, L. Saal-Bauernschubert, and S. Jablonka. 2017. BDNF/trkB induction of calcium transients through $Ca_v2.2$ calcium channels in motoneurons corresponds to F-actin assembly and growth cone formation on β2-chain laminin (221). *Front. Mol. Neurosci.* 10:346. https://doi.org/10.3389/fnmol.2017.00346

Du, J., L. Feng, F. Yang, and B. Lu. 2000. Activity- and Ca(2+)-dependent modulation of surface expression of brain-derived neurotrophic factor receptors in hippocampal neurons. *J. Cell Biol.* 150:1423–1434. https://doi.org/10.1083/jcb.150.6.1423

Ebendal, T. 1992. Function and evolution in the NGF family and its receptors. *J. Neurosci. Res.* 32:461–470. https://doi.org/10.1002/jnr.490320402

Edgar, R., M. Domrachev, and A.E. Lash. 2002. Gene expression omnibus: NCBI gene expression and hybridization array data repository. *Nucleic Acids Res.* 30:207–210. https://doi.org/10.1093/nar/30.1.207

Fletcher, E.V., C.M. Simon, J.G. Pagiazitis, J.I. Chalif, A. Vukojicic, E. Drobac, X. Wang, and G.Z. Mentis. 2017. Reduced sensory synaptic excitation impairs motor neuron function via Kv2.1 in spinal muscular atrophy. *Nat. Neurosci.* 20:905–916. https://doi.org/10.1038/nn.4561

Garbett, D., A. Bisaria, C. Yang, D.G. McCarthy, A. Hayer, W.E. Moerner, T.M. Svitkina, and T. Meyer. 2020. T-Plastin reinforces membrane protrusions to bridge matrix gaps during cell migration. *Nat. Commun.* 11: 4818. https://doi.org/10.1038/s41467-020-18586-3

Giesemann, T., S. Rathke-Hartlieb, M. Rothkegel, J.W. Bartsch, S. Buchmeier, B.M. Jockusch, and H. Jockusch. 1999. A role for polyproline motifs in the spinal muscular atrophy protein SMN. Profilins bind to and colocalize with smn in nuclear gems. *J. Biol. Chem.* 274:37908–37914. https://doi.org/10.1074/jbc.274.53.37908

Giganti, A., J. Plastino, B. Janji, M. Van Troys, D. Lentz, C. Ampe, C. Sykes, and E. Friederich. 2005. Actin-filament cross-linking protein T-plastin increases Arp2/3-mediated actin-based movement. *J. Cell Sci.* 118: 1255–1265. https://doi.org/10.1242/jcs.01698

Hao, T., M. Wolman, M. Granato, and C.E. Beattie. 2012. Survival motor neuron affects plastin 3 protein levels leading to motor defects. *J. Neurosci.* 32:5074–5084. https://doi.org/10.1523/JNEUROSCI.5808-11.2012

Henderson, C.E., H.S. Phillips, R.A. Pollock, A.M. Davies, C. Lemeulle, M. Armanini, L. Simmons, B. Moffet, R.A. Vandlen, L. Simpson LC corrected to Simmons, et al. 1994. GDNF: A potent survival factor for motoneurons present in peripheral nerve and muscle. *Science*. 266: 1062–1064. https://doi.org/10.1126/science.7973664

Hensel, N., and P. Claus. 2018. The actin cytoskeleton in SMA and ALS: How does it contribute to motoneuron degeneration? *Neuroscientist*. 24: 54–72. https://doi.org/10.1177/1073858417705059

Hosseinibarkooie, S., M. Peters, L. Torres-Benito, R.H. Rastetter, K. Hupperich, A. Hoffmann, N. Mendoza-Ferreira, A. Kaczmarek, E. Janzen, J. Milbradt, et al. 2016. The power of human protective modifiers: PLS3 and CORO1C unravel impaired endocytosis in spinal muscular atrophy and rescue SMA phenotype. *Am. J. Hum. Genet.* 99:647–665. https://doi.org/10.1016/j.ajhg.2016.07.014

Huang, W., B.T. Sherman, and R.A. Lempicki. 2009. Systematic and integrative analysis of large gene lists using DAVID bioinformatics resources. *Nat. Protoc.* 4:44–57. https://doi.org/10.1038/nprot.2008.211

Hughes, R.A., M. Sendtner, and H. Thoenen. 1993. Members of several gene families influence survival of rat motoneurons in vitro and in vivo. *J. Neurosci. Res.* 36:663–671. https://doi.org/10.1002/jnr.490360607

Iwata, R., and P. Vanderhaeghen. 2021. Regulatory roles of mitochondria and metabolism in neurogenesis. *Curr. Opin. Neurobiol.* 69:231–240. https://doi.org/10.1016/j.conb.2021.05.003

Jablonka, S., M. Beck, B.D. Lechner, C. Mayer, and M. Sendtner. 2007. Defective Ca^{2+} channel clustering in axon terminals disturbs excitability in motoneurons in spinal muscular atrophy. *J. Cell Biol.* 179:139–149. https://doi.org/10.1083/jcb.200703187

Karpova, T.S., K. Tatchell, and J.A. Cooper. 1995. Actin filaments in yeast are unstable in the absence of capping protein or fimbrin. *J. Cell Biol.* 131: 1483–1493. https://doi.org/10.1083/jcb.131.6.1483

Kong, L., D.O. Valdivia, C.M. Simon, C.W. Hassinan, N. Delestrée, D.M. Ramos, J.H. Park, C.M. Pilato, X. Xu, M. Crowder, et al. 2021. Impaired prenatal motor axon development necessitates early therapeutic intervention in severe SMA. *Sci. Transl. Med.* 13:13. https://doi.org/10.1126/scitranslmed.abb6871

Kowiański, P., G. Lietzau, E. Czuba, M. Waśkow, A. Steliga, and J. Moryś. 2018. BDNF: A key factor with multipotent impact on brain signaling and synaptic plasticity. *Cell. Mol. Neurobiol.* 38:579–593. https://doi.org/10.1007/s10571-017-0510-4

Le, T.T., L.T. Pham, M.E. Butchbach, H.L. Zhang, U.R. Monani, D.D. Coovert, T.O. Gavrilina, L. Xing, G.J. Bassell, and A.H. Burghes. 2005. SMNDelta7, the major product of the centromeric survival motor neuron (SMN2) gene, extends survival in mice with spinal muscular atrophy and associates with full-length SMN. *Hum. Mol. Genet.* 14:845–857. https://doi.org/10.1093/hmg/ddi078

Lee, C.W., E.A. Vitriol, S. Shim, A.L. Wise, R.P. Velayutham, and J.Q. Zheng. 2013. Dynamic localization of G-actin during membrane protrusion in neuronal motility. *Curr. Biol.* 23:1046–1056. https://doi.org/10.1016/j.cub.2013.04.057

Lee, K., J.L. Gallop, K. Rambani, and M.W. Kirschner. 2010. Self-assembly of filopodia-like structures on supported lipid bilayers. *Science*. 329: 1341–1345. https://doi.org/10.1126/science.1191710

Lefebvre, S., P. Burlet, Q. Liu, S. Bertrandy, O. Clermont, A. Munnich, G. Dreyfuss, and J. Melki. 1997. Correlation between severity and SMN protein level in spinal muscular atrophy. *Nat. Genet.* 16:265–269. https://doi.org/10.1038/ng0797-265

Lin, T.W., S.C. Harward, Y.Z. Huang, and J.O. McNamara. 2020. Targeting BDNF/TrkB pathways for preventing or suppressing epilepsy. *Neuropharmacology*. 167:107734. https://doi.org/10.1016/j.neuropharm.2019.107734

Lopez-Manzaneda, M., J. Franco-Espin, R. Tejero, R. Cano, and L. Tabares. 2021. Calcium is reduced in presynaptic mitochondria of motor nerve terminals during neurotransmission in SMA mice. *Hum. Mol. Genet.* 30: 629–643. https://doi.org/10.1093/hmg/ddab065

Lyon, A.N., R.H. Pineda, L.T. Hao, E. Kudryashova, D.S. Kudryashov, and C.E. Beattie. 2013. Calcium binding is essential for plastin 3 function in Smn-deficient motoneurons. *Hum. Mol. Genet.* 23:1990–2004. https://doi.org/10.1093/hmg/ddt595

McGovern, V.L., A. Massoni-Laporte, X. Wang, T.T. Le, H.T. Le, C.E. Beattie, M.M. Rich, and A.H. Burghes. 2015. Plastin 3 expression does not modify spinal muscular atrophy severity in the Δ7 SMA mouse. *PLoS One*. 10:e0132364. https://doi.org/10.1371/journal.pone.0132364

Mentis, G.Z., D. Blivis, W. Liu, E. Drobac, M.E. Crowder, L. Kong, F.J. Alvarez, C.J. Sumner, and M.J. O'Donovan. 2011. Early functional impairment of sensory-motor connectivity in a mouse model of spinal muscular atrophy. *Neuron*. 69:453–467. https://doi.org/10.1016/j.neuron.2010.12.032

Meyer-Franke, A., G.A. Wilkinson, A. Kruttgen, M. Hu, E. Munro, M.G. Hanson Jr, L.F. Reichardt, and B.A. Barres. 1998. Depolarization and cAMP elevation rapidly recruit TrkB to the plasma membrane of CNS neurons. *Neuron*. 21:681–693. https://doi.org/10.1016/S0896-6273(00)80586-3

Monani, U.R., M. Sendtner, D.D. Coovert, D.W. Parsons, C. Andreassi, T.T. Le, S. Jablonka, B. Schrank, W. Rossoll, T.W. Prior, et al. 2000. The human centromeric survival motor neuron gene (SMN2) rescues embryonic lethality in Smn(−/−) mice and results in a mouse with spinal muscular atrophy. *Hum. Mol. Genet.* 9:333–339. https://doi.org/10.1093/hmg/9.3.333

Moradi, M., R. Sivadasan, L. Saal, P. Lüningschrör, B. Dombert, R.J. Rathod, D.C. Dieterich, R. Blum, and M. Sendtner. 2017. Differential roles of α-, β-, and γ-actin in axon growth and collateral branch formation in motoneurons. *J. Cell Biol.* 216:793–814. https://doi.org/10.1083/jcb.201604117

Nölle, A., A. Zeug, J. van Bergeijk, L. Tönges, R. Gerhard, H. Brinkmann, S. Al Rayes, N. Hensel, Y. Schill, D. Apkhazava, et al. 2011. The spinal muscular atrophy disease protein SMN is linked to the Rho-kinase pathway via profilin. *Hum. Mol. Genet.* 20:4865–4878. https://doi.org/10.1093/hmg/ddr425

Oprea, G.E., S. Kröber, M.L. McWhorter, W. Rossoll, S. Müller, M. Krawczak, G.J. Bassell, C.E. Beattie, and B. Wirth. 2008. Plastin 3 is a protective modifier of autosomal recessive spinal muscular atrophy. *Science*. 320: 524–527. https://doi.org/10.1126/science.1155085

Palasz, E., A. Wysocka, A. Gasiorowska, M. Chalimoniuk, W. Niewiadomski, and G. Niewiadomska. 2020. BDNF as a promising therapeutic agent in Parkinson's disease. *Int. J. Mol. Sci.* 21:21. https://doi.org/10.3390/ijms21031170

Pennica, D., V. Arce, T.A. Swanson, R. Vejsada, R.A. Pollock, M. Armanini, K. Dudley, H.S. Phillips, A. Rosenthal, A.C. Kato, and C.E. Henderson. 1996. Cardiotrophin-1, a cytokine present in embryonic muscle, supports long-term survival of spinal motoneurons. *Neuron.* 17:63–74. https://doi.org/10.1016/S0896-6273(00)80281-0

Pradhan, J., P.G. Noakes, and M.C. Bellingham. 2019. The role of altered BDNF/TrkB signaling in amyotrophic lateral sclerosis. *Front. Cell. Neurosci.* 13:368. https://doi.org/10.3389/fncel.2019.00368

Rehberg, M., A. Lepier, B. Solchenberger, P. Osten, and R. Blum. 2008. A new non-disruptive strategy to target calcium indicator dyes to the endoplasmic reticulum. *Cell Calcium.* 44:386–399. https://doi.org/10.1016/j.ceca.2008.02.002

Reichardt, L.F. 2006. Neurotrophin-regulated signalling pathways. *Philos. Trans. R. Soc. Lond. B Biol. Sci.* 361:1545–1564. https://doi.org/10.1098/rstb.2006.1894

Rohrer, B., J.I. Korenbrot, M.M. LaVail, L.F. Reichardt, and B. Xu. 1999. Role of neurotrophin receptor TrkB in the maturation of rod photoreceptors and establishment of synaptic transmission to the inner retina. *J. Neurosci.* 19:8919–8930. https://doi.org/10.1523/JNEUROSCI.19-20-08919.1999

Rossoll, W., S. Jablonka, C. Andreassi, A.K. Kröning, K. Karle, U.R. Monani, and M. Sendtner. 2003. Smn, the spinal muscular atrophy-determining gene product, modulates axon growth and localization of beta-actin mRNA in growth cones of motoneurons. *J. Cell Biol.* 163:801–812. https://doi.org/10.1083/jcb.200304128

Rossoll, W., A.K. Kröning, U.M. Ohndorf, C. Steegborn, S. Jablonka, and M. Sendtner. 2002. Specific interaction of smn, the spinal muscular atrophy determining gene product, with hnRNP-R and gry-rbp/hnRNP-Q: A role for smn in RNA processing in motor axons? *Hum. Mol. Genet.* 11:93–105. https://doi.org/10.1093/hmg/11.1.93

Ruiz, R., J.J. Casañas, L. Torres-Benito, R. Cano, and L. Tabares. 2010. Altered intracellular Ca^{2+} homeostasis in nerve terminals of severe spinal muscular atrophy mice. *J. Neurosci.* 30:849–857. https://doi.org/10.1523/JNEUROSCI.4496-09.2010

Saal, L., M. Briese, S. Kneitz, M. Glinka, and M. Sendtner. 2014. Subcellular transcriptome alterations in a cell culture model of spinal muscular atrophy point to widespread defects in axonal growth and presynaptic differentiation. *RNA.* 20:1789–1802. https://doi.org/10.1261/rna.047373.114

Sarmiere, P.D., and J.R. Bamburg. 2004. Regulation of the neuronal actin cytoskeleton by ADF/cofilin. *J. Neurobiol.* 58:103–117. https://doi.org/10.1002/neu.10267

Sendtner, M., B. Holtmann, R. Kolbeck, H. Thoenen, and Y.A. Barde. 1992a. Brain-derived neurotrophic factor prevents the death of motoneurons in newborn rats after nerve section. *Nature.* 360:757–759. https://doi.org/10.1038/360757a0

Sendtner, M., H. Schmalbruch, K.A. Stockli, P. Carroll, G.W. Kreutzberg, and H. Thoenen. 1992b. Ciliary neurotrophic factor prevents degeneration of motor neurons in mouse mutant progressive motor neuronopathy. *Nature.* 358:502–504. https://doi.org/10.1038/358502a0

Shinomiya, H. 2012. Plastin family of actin-bundling proteins: Its functions in leukocytes, neurons, intestines, and cancer. *Int. J. Cell Biol.* 2012:213492. https://doi.org/10.1155/2012/213492

Simon, C.M., B. Blanco-Redondo, J.M. Buettner, J.G. Pagiazitis, E.V. Fletcher, J.K. Sime Longang, and G.Z. Mentis. 2021. Chronic pharmacological increase of neuronal activity improves sensory-motor dysfunction in spinal muscular atrophy mice. *J. Neurosci.* 41:376–389. https://doi.org/10.1523/JNEUROSCI.2142-20.2020

Simon, C.M., Y. Dai, M. Van Alstyne, C. Koutsioumpa, J.G. Pagiazitis, J.I. Chalif, X. Wang, J.E. Rabinowitz, C.E. Henderson, L. Pellizzoni, and G.Z. Mentis. 2017. Converging mechanisms of p53 activation drive motor neuron degeneration in spinal muscular atrophy. *Cell Rep.* 21:3767–3780. https://doi.org/10.1016/j.celrep.2017.12.003

Skau, C.T., D.S. Courson, A.J. Bestul, J.D. Winkelman, R.S. Rock, V. Sirotkin, and D.R. Kovar. 2011. Actin filament bundling by fimbrin is important for endocytosis, cytokinesis, and polarization in fission yeast. *J. Biol. Chem.* 286:26964–26977. https://doi.org/10.1074/jbc.M111.239004

Smith, B.N., C. Vance, E.L. Scotter, C. Troakes, C.H. Wong, S. Topp, S. Maekawa, A. King, J.C. Mitchell, K. Lund, et al. 2015. Novel mutations support a role for Profilin 1 in the pathogenesis of ALS. *Neurobiol. Aging.* 36:1602–1627.e1617. https://doi.org/10.1016/j.neurobiolaging.2014.10.032

Stevenson, R.P., D. Veltman, and L.M. Machesky. 2012. Actin-bundling proteins in cancer progression at a glance. *J. Cell Sci.* 125:1073–1079. https://doi.org/10.1242/jcs.093799

Suraneni, P., B. Rubinstein, J.R. Unruh, M. Durnin, D. Hanein, and R. Li. 2012. The Arp2/3 complex is required for lamellipodia extension and directional fibroblast cell migration. *J. Cell Biol.* 197:239–251. https://doi.org/10.1083/jcb.201112113

Tanaka, Y., T. Nonaka, G. Suzuki, F. Kametani, and M. Hasegawa. 2016. Gain-of-function profilin 1 mutations linked to familial amyotrophic lateral sclerosis cause seed-dependent intracellular TDP-43 aggregation. *Hum. Mol. Genet.* 25:1420–1433. https://doi.org/10.1093/hmg/ddw024

Tejero, R., S. Balk, J. Franco-Espin, J. Ojeda, L. Hennlein, H. Drexl, B. Dombert, J.D. Clausen, L. Torres-Benito, L. Saal-Bauernschubert, et al. 2020. R-roscovitine improves motoneuron function in mouse models for spinal muscular atrophy. *iScience.* 23:100826. https://doi.org/10.1016/j.isci.2020.100826

Tejero, R., M. Lopez-Manzaneda, S. Arumugam, and L. Tabares. 2016. Synaptotagmin-2, and -1, linked to neurotransmission impairment and vulnerability in Spinal Muscular Atrophy. *Hum.Mol.Genet.* 25:4703–4716. https://doi.org/10.1093/hmg/ddw297

Torres-Benito, L., M.F. Neher, R. Cano, R. Ruiz, and L. Tabares. 2011. SMN requirement for synaptic vesicle, active zone and microtubule postnatal organization in motor nerve terminals. *PLoS One.* 6:e26164. https://doi.org/10.1371/journal.pone.0026164

Welch, M.D., A.H. DePace, S. Verma, A. Iwamatsu, and T.J. Mitchison. 1997. The human Arp2/3 complex is composed of evolutionarily conserved subunits and is localized to cellular regions of dynamic actin filament assembly. *J. Cell Biol.* 138:375–384. https://doi.org/10.1083/jcb.138.2.375

Wiese, S., T. Herrmann, C. Drepper, S. Jablonka, N. Funk, A. Klausmeyer, M.L. Rogers, R. Rush, and M. Sendtner. 2010. Isolation and enrichment of embryonic mouse motoneurons from the lumbar spinal cord of individual mouse embryos. *Nat. Protoc.* 5:31–38. https://doi.org/10.1038/nprot.2009.193

Witke, W. 2004. The role of profilin complexes in cell motility and other cellular processes. *Trends Cell Biol.* 14:461–469. https://doi.org/10.1016/j.tcb.2004.07.003

Wolff, L., E.A. Strathmann, I. Müller, D. Mählich, C. Veltman, A. Niehoff, and B. Wirth. 2021. Plastin 3 in health and disease: A matter of balance. *Cell. Mol. Life Sci.* 78:5275–5301. https://doi.org/10.1007/s00018-021-03843-5

Wu, C., S.B. Asokan, M.E. Berginski, E.M. Haynes, N.E. Sharpless, J.D. Griffith, S.M. Gomez, and J.E. Bear. 2012a. Arp2/3 is critical for lamellipodia and response to extracellular matrix cues but is dispensable for chemotaxis. *Cell.* 148:973–987. https://doi.org/10.1016/j.cell.2011.12.034

Wu, C.H., C. Fallini, N. Ticozzi, P.J. Keagle, P.C. Sapp, K. Piotrowska, P. Lowe, M. Koppers, D. McKenna-Yasek, D.M. Baron, et al. 2012b. Mutations in the profilin 1 gene cause familial amyotrophic lateral sclerosis. *Nature.* 488:499–503. https://doi.org/10.1038/nature11280

Yano, H., I. Ninan, H. Zhang, T.A. Milner, O. Arancio, and M.V. Chao. 2006a. BDNF-mediated neurotransmission relies upon a myosin VI motor complex. *Nat. Neurosci.* 9:1009–1018. https://doi.org/10.1038/nn1730

Supplemental material

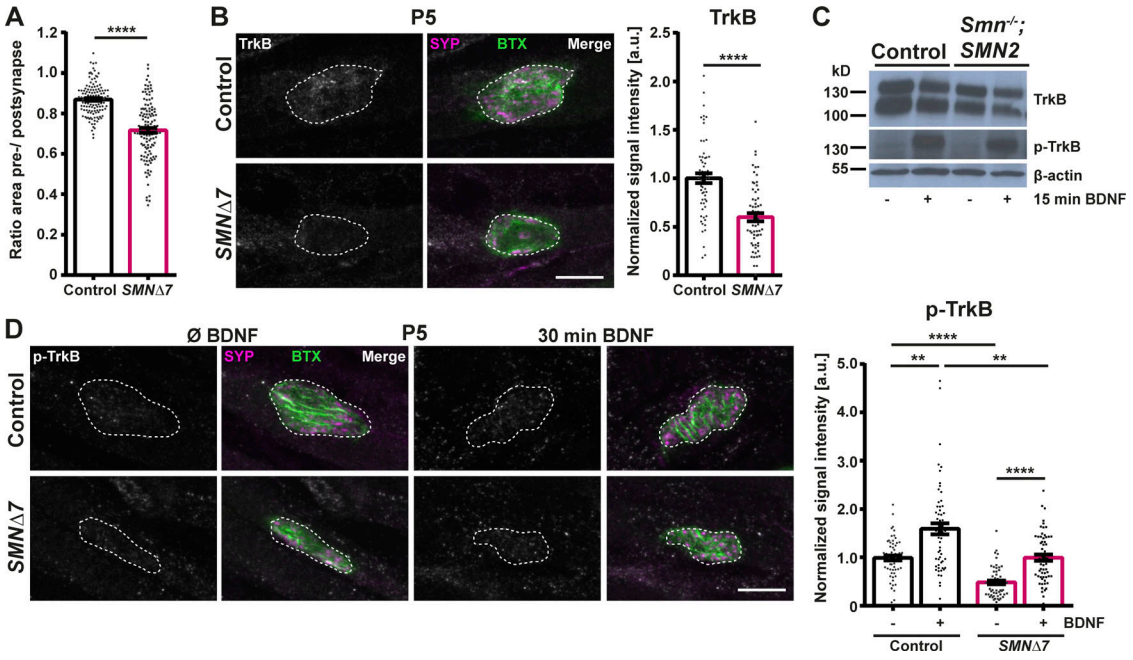

Figure S1. **Disturbed TrkB localization and phosphorylation upon BDNF stimulation are detected in Smn-deficient axon terminals. (A)** Ratio of the area of the presynapse (through Synaptophysin-1 [SYP]) vs. postsynapse (ACh receptors through Bungarotoxin [BTX]) of NMJs in the *Transversus abdominis anterior* (TVA) of control and *SMNΔ7* P10 animals (N = 4, *n* = 130; two-tailed unpaired *t* test, ****P ≤ 0.0001). **(B)** NMJs in the TVA muscle in control and *SMNΔ7* P5 animals stained against TrkB (gray), SYP (magenta) and BTX (green), scale bar: 10 µm. Dotted line depicts outline of the presynapse (SYP signal). Normalized mean gray values of TrkB (N = 4, *n* = 62; Two-tailed unpaired *t* test, ****P ≤ 0.0001). **(C)** Western blot analysis of TrkB and p-TrkB levels in whole-cell lysates of control and $Smn^{-/-}$;*SMN2* motoneurons that were unstimulated or 15 min BDNF stimulated. β-actin was used as loading control. **(D)** Unstimulated and 30 min BDNF stimulated NMJs in the TVA muscle of control and *SMNΔ7* P5 animals stained against p-TrkB (gray), SYP (magenta), and BTX (green), scale bar: 10 µm. Dotted line depicts outline of the presynapse (SYP signal). Normalized mean gray values of p-TrkB (N = 3, *n* = 60; ANOVA Kruskal–Wallis, **P ≤ 0.01; ****P ≤ 0.0001). Data are presented as scatter dot plot with bar. Bars represent the mean ± SEM. Source data are available for this figure: SourceData FS1.

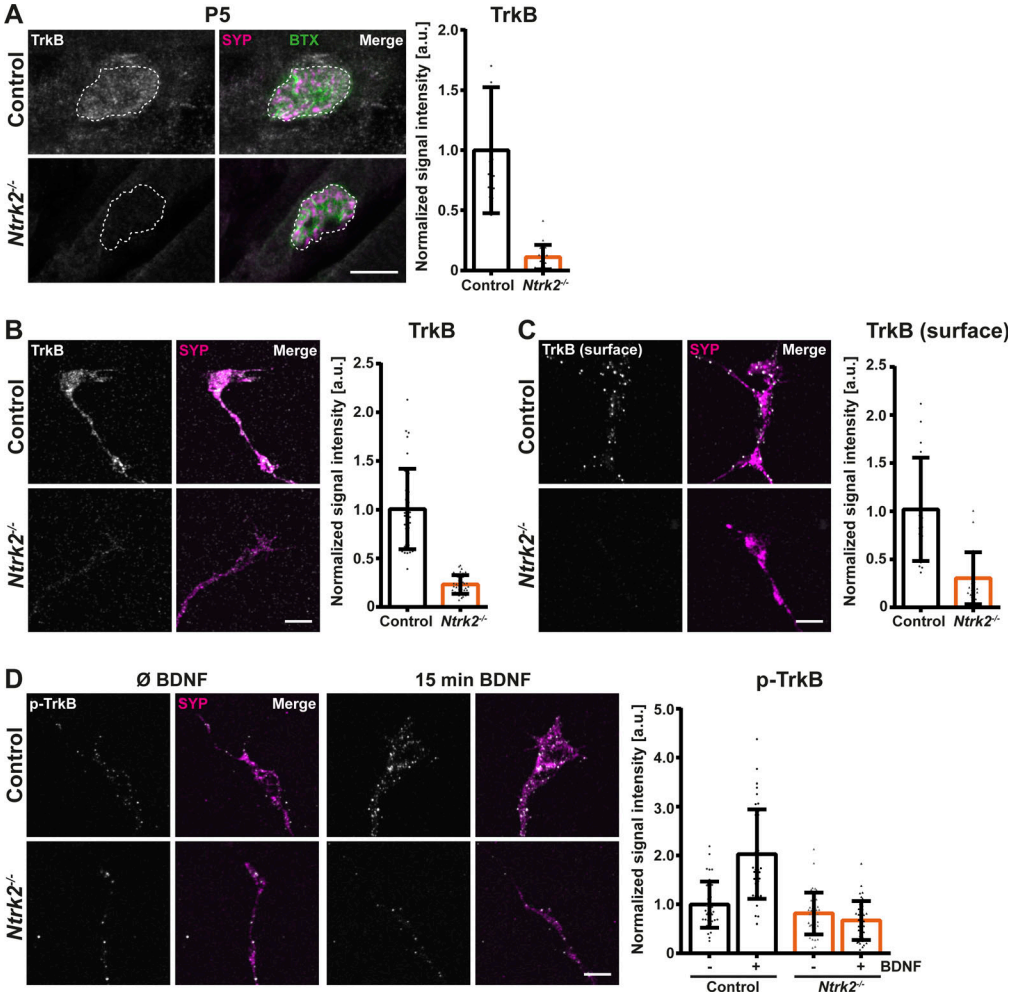

Figure S2. **TrkB and p-TrkB antibody specificity in TrkB-deficient neuromuscular junctions and motoneuron terminals. (A)** NMJs in the *Transversus abdominis anterior* (TVA) of control and *Ntrk2*$^{-/-}$ P5 animals stained against TrkB (gray), Synaptophysin-1 (SYP, magenta), and postsynaptic ACh receptors (BTX, green), scale bar: 10 µm. Dotted line depicts outline of the presynapse (SYP signal). Normalized mean gray values of TrkB (N = 2, *n* = 24). **(B)** Growth cones from control and *Ntrk2*$^{-/-}$ motoneurons stained against TrkB (gray) and SYP (magenta); scale bar: 5 µm. Normalized mean gray values of TrkB (N = 1, *n* = 40). **(C)** Growth cones from control and *Ntrk2*$^{-/-}$ motoneurons stained against surface TrkB (gray) and SYP (magenta); scale bar: 5 µm. Normalized mean gray values of surface TrkB (N = 1, *n* = 20). **(D)** Growth cones from control and *Ntrk2*$^{-/-}$ motoneurons unstimulated and 15 min BDNF stimulated stained against p-TrkB (gray) and SYP (magenta); scale bar: 5 µm. Normalized mean gray values of p-TrkB (N = 2, *n* = 40). Data are presented as scatter dot plot with bar. Bars represent the mean ± SD.

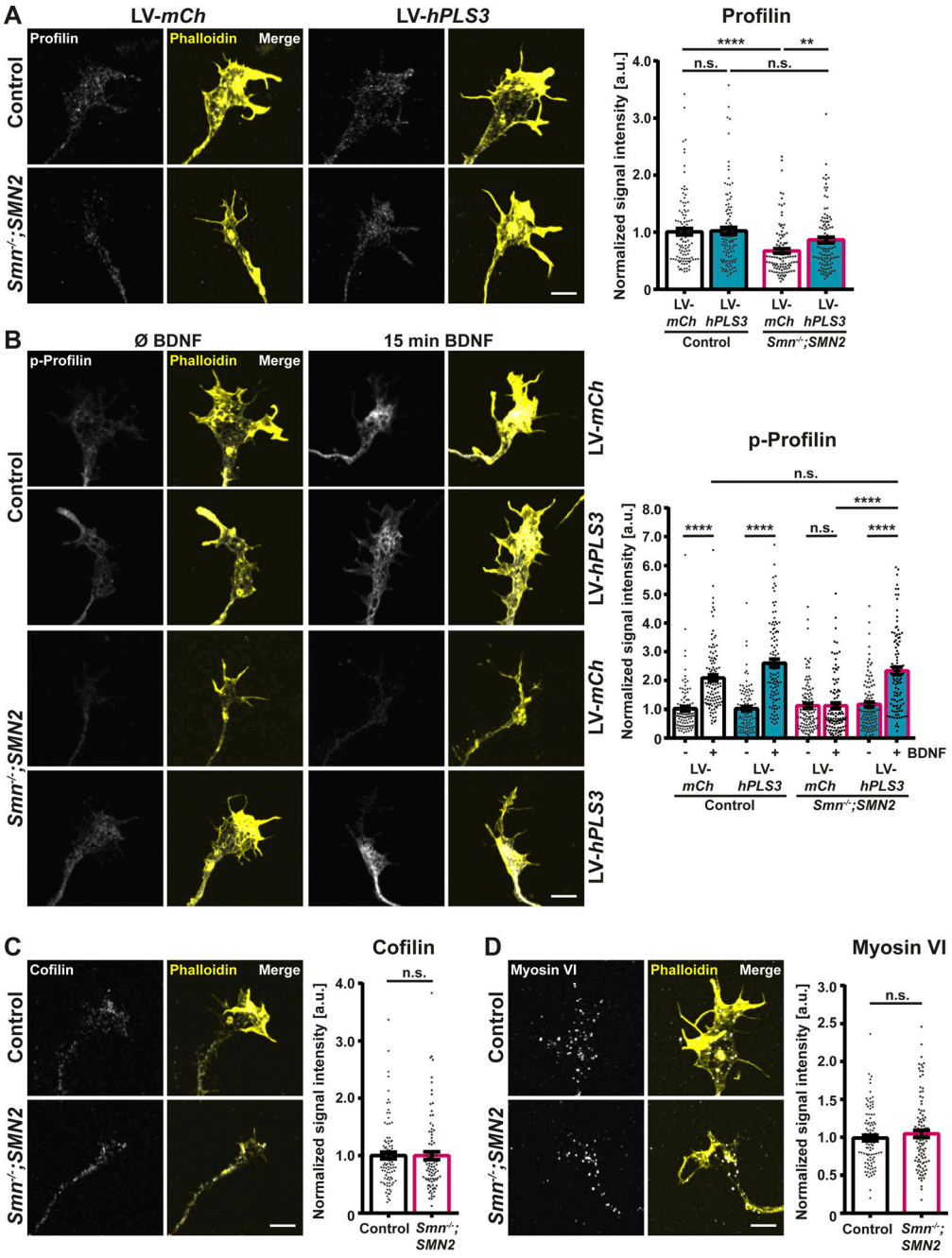

Figure S3. **Overexpression of hPLS3 improves profilin levels and its phosphorylation in Smn-deficient axon terminals. (A)** LV-*mCh* and LV-*hPLS3* transduced control and *Smn*$^{-/-}$;*SMN2* growth cones stained against profilin (gray) and F-actin (Phalloidin, yellow). Normalized mean gray values of profilin (N = 3, *n* = 110; ANOVA Kruskal–Wallis, **P ≤ 0.01; ****P ≤ 0.0001). **(B)** Unstimulated or 15 min BDNF stimulated growth cones from control and *Smn*$^{-/-}$;*SMN2* motoneurons transduced with LV-*mCh* and LV-*hPLS3* stained against p-profilin (gray) and F-actin (Phalloidin, yellow). Normalized mean gray values of p-profilin (N = 3, *n* = 105; ANOVA Kruskal–Wallis, ****P ≤ 0.0001). **(C)** Control and *Smn*$^{-/-}$;*SMN2* growth cones stained against cofilin (gray) and F-actin (Phalloidin, yellow). Normalized mean gray values of cofilin (N = 3, *n* = 90; U-Mann–Whitney). **(D)** Control and *Smn*$^{-/-}$;*SMN2* growth cones stained against myosin VI (gray) and F-actin (Phalloidin, yellow). Normalized mean gray values of myosin VI (N = 3, *n* = 100; U-Mann–Whitney). Data are presented as scatter dot plot with bar. Bars represent the mean ± SEM. Scale bars: 5 µm.

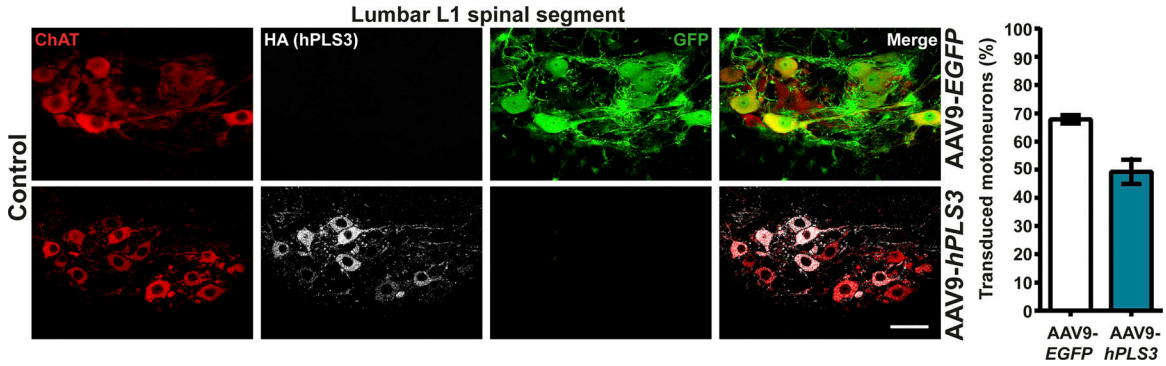

Figure S4. **Virus-mediated hPLS3overexpression in L1 spinal segment motoneurons.** Motoneuron soma within the L1 lumbar spinal segment of P10 control animals injected with AAV9-*EGFP* or AAV9-*hPLS3*, stained against choline acetyltransferase (ChAT, red), HA (gray) and GFP (green), scale bar: 50 µm. Quantification of the percentage of GFP (AAV9-*EGFP*) or HA (AAV9-*hPLS3*)-expressing motoneurons (n = 3/4). Data are presented as mean ± SD.

Video 1. **TrkB-GFP movements upon cAMP stimulation within axon terminals of LV-*mCh* control motoneurons.** Time-laps videos were recorded from DIV7 control motoneurons co-transduced with LV-*mCh* and LV-*TrkB-GFP* during a 30 min 100 µM 8-CPT-cAMP stimulation using an epifluorescence microscope acquiring images at a 2.5 s interval over a time period of 10 min. TrkB-GFP movements (gray) are shown at a display rate of 7 frames per second.

Video 2. **TrkB-GFP movements upon cAMP stimulation within axon terminals of LV-*mCh Smn*$^{-/-}$*;SMN2* motoneurons.** Time-laps videos were recorded from DIV7 *Smn*$^{-/-}$*;SMN2* motoneurons co-transduced with LV-*mCh* and LV-*TrkB-GFP* (gray) during a 30 min 100 µM 8-CPT-cAMP stimulation using an epifluorescence microscope acquiring images at a 2.5 s interval over a time period of 10 min. TrkB-GFP movements (gray) are shown at a display rate of 7 frames per second.

Video 3. **TrkB-GFP movements upon cAMP stimulation within axon terminals of LV-*hPLS3 Smn*$^{-/-}$*;SMN2* motoneurons.** Time-lapse videos were recorded from DIV7 *Smn*$^{-/-}$*;SMN2* motoneurons co-transduced with LV-*hPLS3* and LV-*TrkB-GFP* (gray) during a 30 min 100 µM 8-CPT-cAMP stimulation using an epifluorescence microscope acquiring images at a 2.5 s interval over a time period of 10 min. TrkB-GFP movements (gray) are shown at a display rate of 7 frames per second.

Provided online are Table S1 and Table S2. Table S1 shows RNA-seq results. Table S2 shows GO term analysis of the differential gene expression in the somatodendritic and axonal compartment of Smn knockdown and GFP-expressing control motoneurons grown in compartmentalized chambers.